UNIVERSITY OF ILLINOIS
URBANA

AERONOMY REPORT NO. 94

CALIBRATION OF THE URBANA LIDAR SYSTEM

by
T. Cerny
C. R. Seeliger, Jr.

August 1, 1980

Library of Congress ISSN 0568-0581

Supported by
National Science Foundation
National Aeronautics and Space Administration

Aeronomy Laboratory
Department of Electrical Engineering
University of Illinois
Urbana, Illinois

UILU-ENG-80 2503

A E R O N O M Y R E P O R T

N O. 94

CALIBRATION OF THE URBANA LIDAR SYSTEM

by

T. Cerny
C. F. Sechrist, Jr.

August 1, 1980

Supported by
National Science Foundation
Grants ATM 78-12308 and ATM 79-20726
National Aeronautics and
Space Administration
Grant NGR 14-005-181

Aeronomy Laboratory
Department of Electrical Engineering
University of Illinois
Urbana, Illinois

ABSTRACT

A method for calibrating data obtained by the Urbana sodium lidar system is presented. First, an expression relating the number of photocounts originating from a specific altitude range to the sodium concentration is developed. This relation is then simplified by normalizing the sodium photocounts with photocounts originating from the Rayleigh region of the atmosphere. To evaluate the calibration expression, the laser linewidth must be known. Therefore, a method for measuring the laser linewidth using a Fabry-Perot interferometer is given. The laser linewidth was found to be 6 ± 2.5 pm. Problems due to photomultiplier tube overloading are discussed. Finally, calibrated data is presented. The sodium column abundance exhibits something close to a sinusoidal variation throughout the year with the winter months showing an enhancement of a factor of 5 to 7 over the summer months.

TABLE OF CONTENTS

LIST OF TABLES

LIST OF FIGURES

1. INTRODUCTION

1.1 *General Lidar Concepts*

The word lidar is an acronym for Light Detection And Ranging. As the name would imply, a lidar system is very similar to a radar system operating at much greater frequencies. Like a radar system, a lidar system is composed of a transmitter and receiver. A lidar transmitter consists of a pulsed laser source sometimes equipped with beam collimating optics. The lidar receiver is comprised of a telescope, a filter to eliminate background light, a detector and signal recording equipment.

For something to be detected by lidar methods, the object must interact with the light in such a manner that enough of the incident light is scattered back to the telescope that it can be detected above the system noise level. For atmospheric lidar, the scattering process is performed by particles and constituents which normally reside in the atmosphere. As a radar target's effectiveness is measured by a radar cross section, an atmospheric particle's ability to produce an echo is given by the particle's scattering cross section. The range from the lidar system to the scatterer is found by measuring the amount of time the light pulse takes to propagate to the scatterer, be scattered and then return to the detection equipment. The range of the scatterer is given by $R = \frac{1}{2}c\Delta t$ where c is the speed of light and Δt is the time interval. The factor of $\frac{1}{2}$ accounts for the two way propagation. It is assumed the scattering process occurred instantaneously, which is not always the case. An example in which the scattering process is not instantaneous would be a resonant scatter from CO_2 at 10.4 μm. The decay rate of this molecule for this transition is around $\frac{1}{3}$ sec.

This chapter will serve as an introduction by briefly reviewing lidar concepts and equipment as well as a description of the sodium layer. Sections 1.2 and 1.3 describe the historical progress of lidar systems and a summary of observed features of the layer respectively. Section 1.4 describes the configuration of the present lidar system located near Urbana, Illinois. The chapter concludes with the objectives and scope of this study in Section 1.5.

1.2 *Lidar Systems and Past Observations*

Lidar, also known as laser radar or optical radar, was first used to study the upper atmosphere in the early 1960's, soon after the birth of the laser. The first configurations were used to study the atmospheric density

profile as well as aerosol layers over a wide altitude range. The laser used with these systems was usually a Q-switched ruby laser. The operating frequency of the transmitter was not a critical factor in these observations, since the scattering mechanisms operate over a wide range of wavelength. A good review of lidar fundamentals and results concerning aerosol content and atmospheric density and composition can be found in *Kent and Wright* [1970].

With the advent of the tunable dye laser, scattering mechanisms which operated on an atomic or molecular resonance method could now be observed. Sodium, an atmospheric constituent which had been observed via airglow measurement techniques [*Hunten*, 1967], was the first species to be observed by resonance scattering [*Bowman et al.*, 1969]. Several groups have become involved in the study of the sodium layer and have reported results concerning the nature and variation of the layer with the backing of an extensive data base [*Simonich et al.*, 1979; *Gibson and Sandford*, 1971; *Megie and Blamont*, 1977].

As equipment improved and the integration time over which a profile was collected was reduced, reports concerning fine structure in the layer were reported [*Kirchhoff and Yamamoto*, 1973; *Boulett et al.*, 1978]. A technique of processing the data using digital filters was developed which aided an observer in seeing the density perturbations in the vertical structure [*Boulett et al.*, 1978]. There is considerable evidence which points to internal atmospheric gravity waves as being the origin of this structure.

Other improvements in the lidar technique include a steerable system which can observe horizontal variations in the layer [*Thomas et al.*, 1977], the study of the potassium layer [*Megie et al.*, 1978], daytime observation [*Gibson and Sandford*, 1972] and observations of the vertical temperature profile [*Blamont et al.*, 1972; *Gibson et al.*, 1979].

1.3 *Sodium Layer Description and Reasons for Study*

Atomic sodium is found over an altitude range of 75 to 105 km above the earth's surface. This altitude range corresponds to the upper mesosphere and lower thermosphere. The boundary between these two regions occurs at the mesopause. The peak of the layer is found somewhere between 83 km to 95 km with a width of from 5 to 12 km. The altitude of the peak can vary greatly over the space of a few hours and is often bifurcated. Figure 1.1 shows data taken near Urbana on November 11-12, 1977 and shows a good deal of

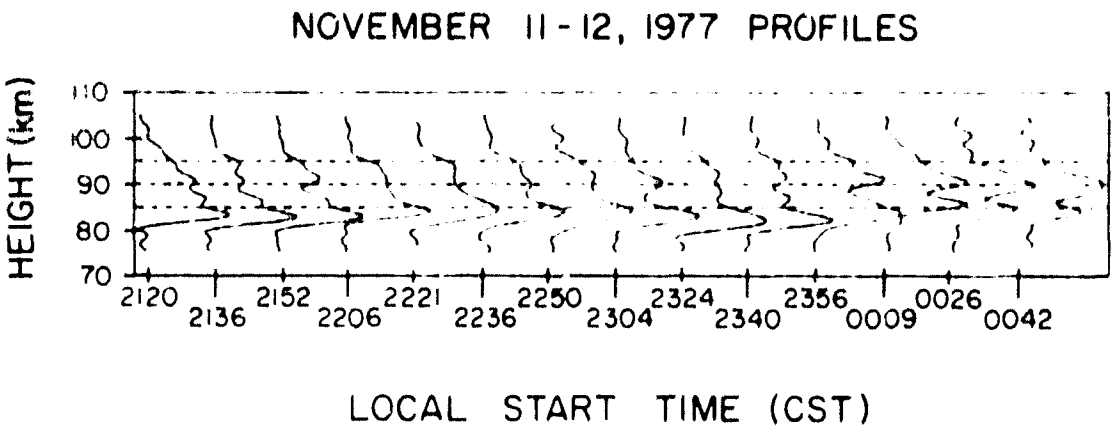

Figure 1.1 Series of profiles of the sodium concentration versus altitude observed on the night of November 11-12, 1977. Note the oscillation of the bottomside of the layer and the formation of a bifurcated layer later in the evening. The second maximum which forms eventually becomes the layer maximum by the end of the evening's observation.

variability. This data was filtered to remove spatial frequencies in the data higher than $(3.5\ km)^{-1}$. The first profile at 2120 CST shows a peak occurring at 83 km. The layer falls off very sharply on the bottomside and slowly decays on the topside. This small scale height, or distance over which the concentration falls by a factor of $1/e$, is commonly observed and is much smaller than the atmospheric scale height. The bottom of the layer undulates up and down over the course of an evening having a period of about 2 hours. At 2356, a second peak forms at 91 km, and in 30 minutes has become the dominant peak of the layer. These rapid variations and steep concentration gradients point towards strong dynamic and chemical forces at play in this layer.

Seasonal variations have been reported by several groups [*Simonich et al.*, 1979; *Megie and Blamont*, 1977; *Gibson and Sandford*, 1971]. They have reported increases in the column abundance during the winter by a factor of 2 to 5 over those observed in the summer. *Simonich et al.* [1979] postulated the variation in the ratio of increase was due to latitude, the stronger winter enhancements occurring at higher latitudes.

The origin of the sodium in the atmosphere is thought to be from meteoric ablation. This is evidenced by the number of other metallic elements which reside in this part of the atmosphere, each of which is commonly found in meteors. Other evidence of a meteoric origin is provided by observed enhancements in the sodium column abundance during meteor showers, some as large at 200% greater than the monthly mean [*Megie and Blamont*, 1977].

There are three major reasons for wanting to study the atmospheric sodium layer. First, the layer itself is important in the neutral and ion chemistry of the region. Although sodium is only a minor constituent at these altitudes, positive sodium ions are a significant species of positive ion and hence affect the charged particle concentration including electron densities. Sporadic-*E* occurrences have been shown to be caused by enhancements of metallic ions, sodium included [*Herrmann et al.*, 1978]. Several authors have offered theories and models of the chemistry of the region with a recent one including cluster ion reactions [*Richter and Sechrist*, 1979].

Secondly, the layer has proven to be an excellent tracer of dynamic effects in this region. Figure 1.1 shows many features which are thought to be due to dynamic effects, especially gravity wave propagation. The sodium

layer should provide information concerning these waves and how they propagate, in the future.

Finally the vertical structure of the atmospheric temperature can be measured in the sodium layer altitude range. There are two methods for making this measurement with lidar techniques. One way is to step a narrow linewidth laser through the sodium line, collecting a photocount profile for each step. This results in an experimental lineshape at several altitudes for the sodium. Since the lineshape of the sodium atoms is temperature dependent, the desired temperature information is deduced by finding the temperature which provides the best fit of a theoretical lineshape to the measured one. The second method involves placing an absorption cell in the received photons path. The absorption through the cell will be dependent on the atmospheric temperature. This measurement is important since temperature information from this region is sparse. It is accessible for *in situ* observation only by rockets.

1.4 *Urbana Lidar System*

Figure 1.2 shows a block diagram of the Urbana lidar system. The transmitter section is dominated by the dye laser. The dye laser used in the Urbana lidar system has been described by *Richter and Weinhart* [1978]. However, a short synopsis of the laser will be presented here. This synopsis will also include new equipment added to the laser since the previous report.

The dye Rhodamine 6G is used as the lasing material at a concentration of 5×10^{-5}M. A solvent of equal amounts of ethanol and distilled water is used mostly for safety purposes. A quenching agent, 1, 3, 5, 7 - cyclooctatetraene is used in the dye mixture at a concentration of 5×10^{-3}M to aid the lasing transition's effectiveness. The dye is continuously circulated through a rod on the laser mainframe at a rate of 1.5 liters/min.

The dye rod lies along the common focus of a bielliptical cavity. Two linear flashlamps having an arc length of 11 inches reside in the two independent foci. The flashlamps are the ablating type operating at a pressure of 6 - 9 Torr of nitrogen. Fresh nitrogen is continuously passed through the lamps by bleeding nitrogen into one end of the flashlamps and pumping it out the other end with a vacuum pump. Excess ablation products are removed from the system in this manner as well, being collected in a flask trap. The flashlamps are continuously water cooled to increase their operating

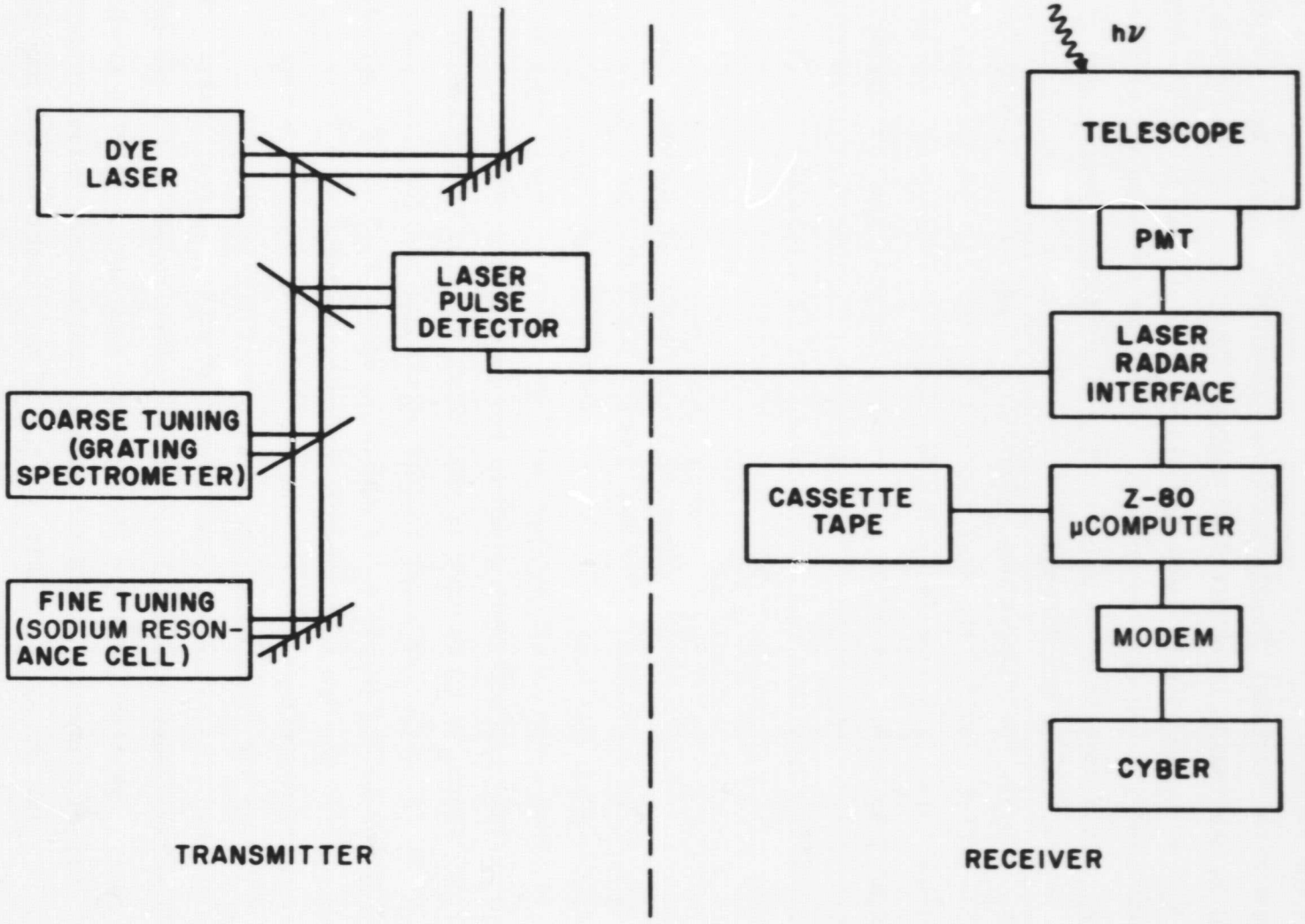

Figure 1.2 Block diagram of the Urbana lidar system. Double lines indicate light paths while single lines represent electrical connections. Angled lines in light path symbolize beamsplitters and mirrors.

life and to prohibit heat gradients from altering the index of refraction of the dye rod. Since the flashlamps create vibrations when they're triggered, care is taken to isolate mechanically the flashlamp setup from the optical rail where the dye rod and cavity optics rest. Energy for the flash is stored in a 5 μF, 25 kV capacitor and is released by pre-ionizing the lamps with a high voltage pulse. The pre-ionizing pulse increases the conduction of the flashlamps allowing the applied voltage from the capacitor to establish a large electric field inte the lamps then flash and release the stored energy.

The dye laser cavity must perform the selection of the operating frequency and sufficiently narrow the linewidth of the output. This is necessary since the dye will lase over a wavelength range of 5 nm. Therefore, the cavity has two frequency selective devices. At the rear of the laser, farthest away from the output end, a grating is placed oriented in the Littrow position. This position implies the desired wavelength has its first order diffracted back along the cavity axis. Clearly, any other wavelength will be directed out of the cavity, thus providing the frequency selection. The current grating has 1800 lines/mm and is cut at a blaze angle such that there is minimum loss into other orders. In front of the grating is located a flat 40% reflective mirror oriented perpendicular to the optical axis. This mirror reduces the optical energies incident on the easily burned grating. These two optical elements together are called a mirror grating combination (MGC). The MGC provides a narrower linewidth and higher reflectivity than the grating alone, aside from the reduced intensity on the grating.

The next optical device on the rail is a Fabry-Perot etalon. An etalon is essentially two plane mirrors adjusted into high tolerance parallelism. This device further narrows the linewidth of the laser and is the other frequency selective device. The two mirrors form an optical resonant cavity, having resonances at wavelengths where the round trip phase shift of a light beam within the cavity is a multiple of 2π. The separation of these resonant wavelengths is denoted as the free spectral range. This concept and other concepts associated with Fabry-Perot devices are discussed in Chapter 3. The free spectral range of the etalon presently in use is 0.6 nm. By changing the angle of incidence at which the beam passes through the etalon,

the effective length of the resonant cavity is changed and the laser frequency is altered. Fine tuning of the laser is effected in this way. On the other side of the dye rod, the output mirror is put into position. The current configuration uses a spherical mirror with a radius of curvature of 6 m and a reflectivity of 55%. A 45-degree folding mirror directs the beam upwards into the atmosphere and completes the rail optics.

Tuning is monitored by a grating spectrometer and a sodium resonance cell. The coarse tuning is performed by using the grating spectrometer with a sodium arc lamp providing a D_1 and D_2 line for reference. Unfortunately, the spectrometer does not have enough resolution to tune the laser output onto the 3 pm wide sodium line. This fine tuning is done by passing a portion of the laser beam through a heated cell filled with sodium vapor. When the laser is at the correct frequency, scatter can be observed as the beam passes through the cell. By maximizing scatter, good tuning can be assured. A picture of the laser mainframe is shown in Figure 1.3.

The receiving system begins with the 1.22-m Fresnel lens telescope. This instrument is described by *Rowlett and Gardner* [1979] in detail. A brief description of it follows for completeness. The telescope consists of the 1.22-m Fresnel lens, a folding mirror to change the optical axis from vertical to horizontal, a field stop iris, a collimating lens, a filter, a focusing lens and finally, a photomultiplier tube (PMT). The collimating lens is necessary to allow proper performance of the interference filter. The PMT is a high gain, low noise unit. The system noise level is dominated instead by background light collected by the telescope.

The output from the PMT goes to the laser radar interface [*Kinter*, 1977]. In the interface is a high speed counter, continually being incremented by pulses from the PMT. The interface begins timing once it has been notified by the laser pulse detector that a shot has begun. After a delay period when the returns begin from an altitude of interest, the counter is periodically sampled. Each sample is stored in a quick access memory location. Once the shot is completed, the data is transferred to a Z-80 microcomputer [*Veitelbaum and Sechrist*, 1979] where the difference between samples is computed and stored. The sampling interval corresponds to a height interval from which the counted photons originated. Therefore, each value stored in the computer represents photons from that range interval or

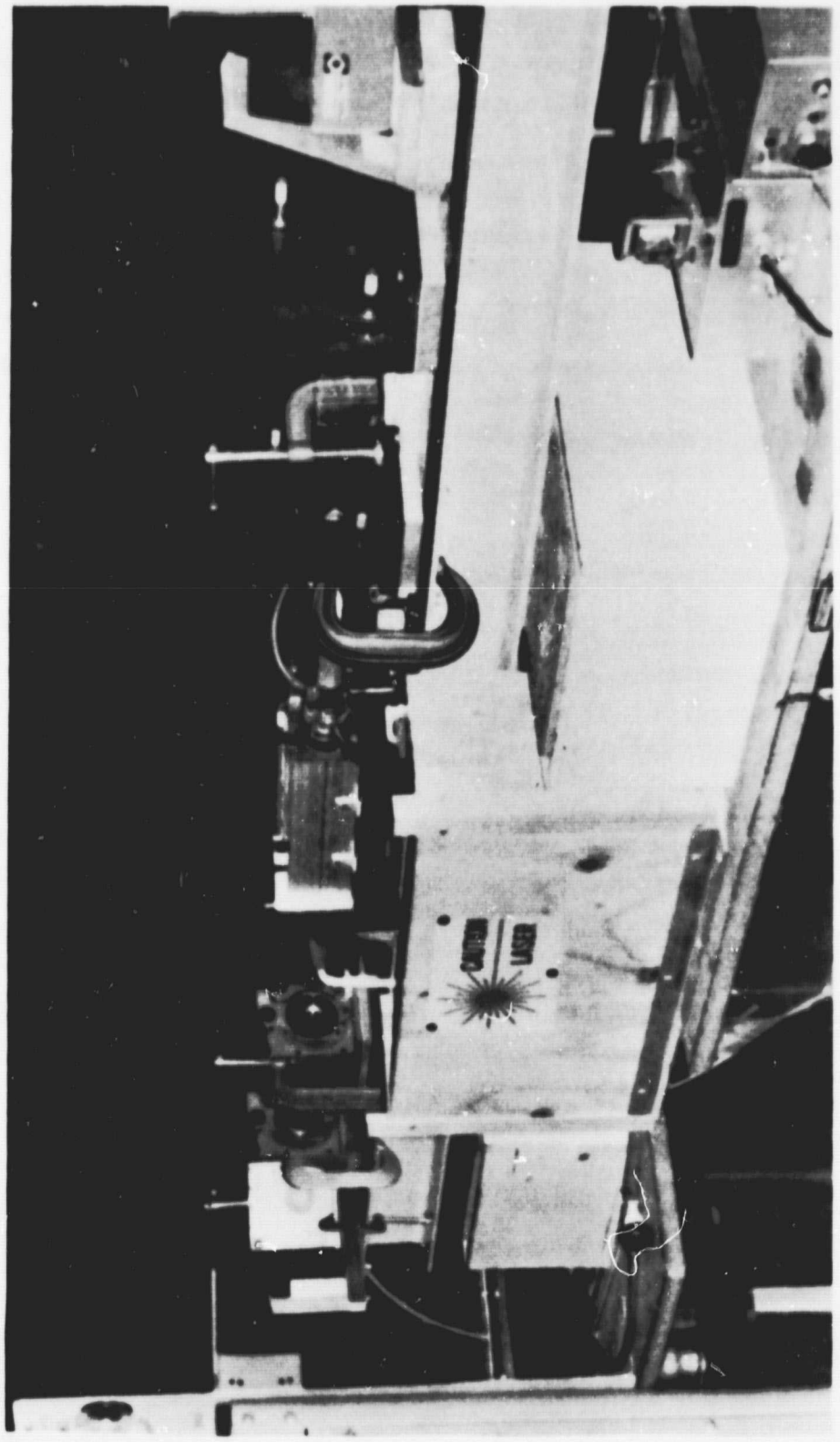

Figure 1.3 Photograph of the optical rail of the Urbana dye laser. Optics and devices on the rail from left to right are the grating, the R = 40% MGC mirror, the etalon, the biellíptical cavity, the R = 55% output mirror and the 45° R_{max} folding mirror.

range bin. In this way, an altitude vs. photocounts profile can be obtained. Very few photons originating from the sodium layer are obtained by one shot. To construct a good, low shot noise profile, range bin values over several shots must be added together or integrated. Usually anywhere between 50 and 300 shots are required for each profile spanning an interval of 5 to 12 minutes of integration time.

Once enough photons for a profile are collected, the data values are stored on cassette tape. After the evenings observation is over, the data are re-read into the computer and transferred over the phone line via a modem to the University of Illinois Cyber 175. At a later date, the data are processed in final form. A table of the parameters of the Urbana lidar system is presented in Table 1.1.

1.5 *Objectives and Scope of This Study*

The objective of this study is to make the necessary measurements and calculations necessary to convert the sodium photocount data into sodium concentration vs. altitude profiles. The concentration value are important factors in the validation of dynamic and chemical models of this region. Calibration also allows profiles to be compared within an evening, from day to day or on a seasonal basis.

The major obstacle preventing the calibration of this system in the past was an unknown value of the laser linewidth. Therefore, a major part of this work was involved with this measurement. Other factors, such as PMT overloading, caused previous methods to be outdated. Finally, the data had to be processed to obtain calibrated data.

Chapter 2 presents the principles and concepts behind the calibration technique. Chapter 3 provides information concerning the linewidth measurement and the theory behind it. Chapter 4 summarizes the PMT overloading problem while experimental results and error analysis are given in Chapter 5. Conclusions and recommendations for further study comprise Chapter 6.

Table 1.1 Values of the current Urbana lidar system parameters.

Parameter	Value
Wavelength	589 nm
Transmitted Bandwidth	6 pm
Laser Beam Divergence (half angle)	<1 mrad
Laser Pulse Energy	50-100 mJ
Pulse Duration	4μs FWHM
Receiver Gate Time	3μs
Receiver Area	1.17 m^2
Receiver Bandwidth	5 nm
Receiver Efficiency	0.05
Receiver Beam Divergence (half angle)	3 mrad
Separation of Receiver and Transmitter	10 m
Repetition Rate	0.5 s^{-1}

2. LIDAR PRINCIPLES AND CALIBRATION TECHNIQUE

2.1 *Introduction*

The previous chapter gave a brief overview of lidar system operation. This chapter analyzes the process by which signal photons are received and counted, in enough detail to be able to quantify the process. A relationship between the observed photocounts and the concentration of the scatterer producing the signal photons is developed. The material is presented more for completeness than for originality, and the development closely parallels the one presented by *Richter and Sechrist* [1978].

Section 2.2 discusses how the major loss mechanisms operate on a light beam propagating through the atmosphere and its relationship to the received signal. Section 2.3 develops the lidar equation, relating photocounts to sodium concentration. The effective scattering cross section and the transmission through the sodium layer are discussed in Sections 2.4 and 2.5, respectively. Each of those terms are used in the calibration calculation. A method of calibration which simplifies the expression derived in Section 2.3 by normalizing the sodium returns to returns from the Rayleigh scattering region of the atmosphere is the topic of Section 2.6. The chapter concludes with a description of the Rayleigh scattering cross section, a quantity used in the normalization process, in Section 2.7.

2.2 *Light Beam Extinction in the Atmosphere*

There are two mechanisms which operate on a light beam to cause it to be attenuated as it propagates through the atmosphere. First, the light can be absorbed by particles with absorbed energy being transferred into some non-optical form of energy. Secondly, the light can be scattered from the beam into another direction. The expression for the intensity of a beam after it has propagated through a media of length ℓ is given by Bouger's Law which is:

$$I = I_0 \exp[-\int_0^{\ell} \beta_{ex}(s)ds] \tag{2.1}$$

where β_{ex} is the extinction coefficient over the path of propagation. The extinction coefficient is made up of two parts, the volume total scattering coefficient β_{sc} and the absorption coefficient β_{ab}, in the following manner:

$$\beta_{ex} = \beta_{sc} + \beta_{ab} \tag{2.2}$$

The term β_{π} is particularly important for lidar systems since it is the source of the signal photons collected by the system. The units for β_{ex}, β_{π} and β_{sb} are in inverse length.

There are four basic types of scattering processes which can contribute to β_{π}. They are Rayleigh, Mie, resonance and Raman scattering. Raman scattering is characterized by a frequency shift in some of the returns. This effect stems from a change in energy levels in an excited molecule and requires the quantum theory to describe. This type of scattering is not important for the Urbana lidar, and so will not be dealt with hereafter. Rayleigh and Mie scattering are caused by the presence of particles in the media of propagation which form inhomogeneities for the propagating fields. Rayleigh scattering theory is a special case of Mie theory, applicable when the radius of the scattering particle satisfies the following relationship:

$$r \leq .03\lambda \tag{2.3}$$

This condition is satisfied by gaseous atmospheric molecules which comprise the air. The Mie theory is applicable to particles such as volcanic and meteoric dust as well as water droplets in clouds. Rayleigh scattering is characterized by equal amounts of scattering into the forward and rear hemisphere of a particle. The forward direction is determined by the incident beams direction. The Rayleigh scattering at right angles to the beam of incidence is strongly polarized. Mie scattering exhibits strong scattering into the direction of propagation. The larger the ratio of radius to wavelength, the stronger the forward scattering will be.

Finally, resonance scattering involves the absorption of a photon by a molecule or atom into an electronic transition and its subsequent spontaneous emission. The emitted photon is at or near the original frequency and travels with equal probability in all directions. This is the mechanism by which the sodium layer is observed.

To be able to quantify further the effectiveness of a scatterer, some assumptions must first be made. For atmospheric scattering, the particles are separated adequately and undergo random motion so that the contributions to the total scattered energy by many particles have no phase differences. This allows the total intensity to be calculated by adding the intensity from each scattering particle. This process is known as independent scattering. Another assumption made due to the low density of air is that of

single scattering. Single scattering implies that a photon is scattered only once. If a photon is scattered two or more times then multiple scattering occurs. Naturally, single scattering results in a much more straightforward manner of describing the scattering process.

Several quantities exist which aid in quantitatively describing the effectiveness of a scatterer. The angular scattering cross section, $\sigma(\theta)$ is defined as the area of impinging flux which is scattered into a unit solid angle in an observation angle, θ. This geometry is diagrammed in Figure 2.1. By this definition, the number of photons scattered from a photon flux Φ into direction θ is given by:

$$N = \Phi\, \sigma(\theta) \text{ photons per steradian} \tag{2.4}$$

The total scattering cross section is another quantity used in scattering theory and is defined as the total area of flux scattered in all directions by the particle. This can be found by integrating $\sigma(\theta)$ over 4π steradians.

Two more commonly used terms are the volume angular scattering coefficient and volume total scattering coefficient. The volume angular scattering coefficient $\beta(\theta)$ is defined as the area of incident flux which is scattered in a direction θ per unit solid angle by a unit volume of scatterers. Under the assumption of independent scatter, this quantity would just be the angular cross section of one scatterer multiplied by the total number of scatterers in the unit volume. This can be expressed as:

$$\beta(\theta) = \sigma(\theta)\rho \tag{2.5}$$

where ρ is the number density of scatterers. The volume total scattering coefficient is the term used in the beginning of this section in Bouger's Law. It is defined as the area of incident flux which is scattered in all directions by a unit volume of scatterers. A value for β can be found by either multiplying σ by the number density of scatterers or by integrating $\beta(\theta)$ over 4π steradians.

Hopefully, these definitions will provide the needed groundwork to understand better the development of the lidar equation in the next section. Sections 2.4 and 2.7 will discuss in more detail values for a resonance and Rayleigh cross section, respectively. Several good references exist to describe scattering in the atmosphere. *McCartney* [1976] is a thorough and highly readable text on the subject while *Van De Hulst* [1957] is a rigorous and often cited resource.

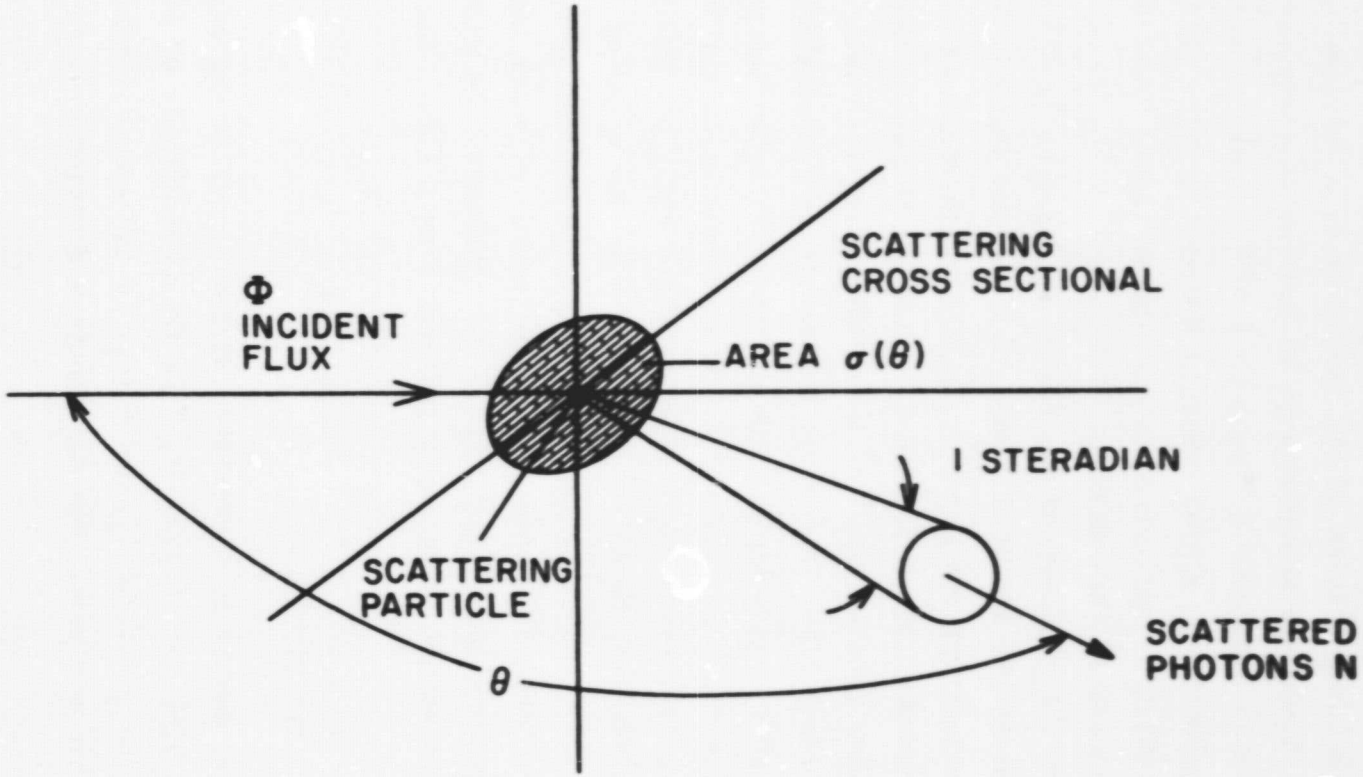

Figure 2.1 Diagram illustrating the defining geometry of a single scatterer for the angular scattering cross sectional area $\sigma(\theta)$. The amount of flux passing through the marked area will be scattered into a unit solid angle in the direction θ. The scattering plane is defined as the plane containing the incident flux line and the line denoting the direction of scatter.

2.3 Lidar Equation Development

The lidar equation relates the received signal obtained from a scattering region to the concentration of the scatterer as a function of several system parameters. There are numerous ways to develop this expression. A very rigorous method is presented by Measures [1977]. Another derivation, given by Richter and Schrider [1978] presents a more intuitive development and gives a result which is applicable to the Urbana lidar. That development will be closely followed in this section.

First, consider the geometry of the system as depicted in Figure 2.2. This system operates in the monostatic mode in which the distance of separation between the transmitter and receiver is negligible compared to the distance at which the photocounts originate. Due to the method the counter on the photomultiplier tube is sampled, the height is divided into intervals of altitude called range bins. The range bin at the bottom of the sodium layer will be denoted as range bin 1. The altitude at the bottom of range bin 1 is z_1, with the center of the range bin occurring at an altitude of $z_1 + \Delta z/2$. Here, Δz represents the thickness of the range bin and is related to the counter sampling time by $\Delta z = \frac{1}{2} c \Delta t$ where c is the speed of light. The notation is easily extended to range bin i for the general case.

Consider now a photon flux impinging on the bottom of range bin i. The flux expression is a function of frequency ν and represents the number of photons per unit area within a frequency interval ν to $\nu + d\nu$. The flux can be expressed as:

$$\Phi(\nu, z_i) = \frac{N_t \, g(\nu)}{A_t(z)} T \tag{2.6}$$

where N_t is the total number of transmitted photons, $g(\nu)$ is the distribution of the transmitted light over frequency, T is the transmission of the beam through the atmosphere to height z_i, and $A_t(z_i)$ is the area illuminated by the laser beam at this altitude. The distribution function $g(\nu)$ is normalized and defined by:

$$\int_0^\infty g(\nu) \, d\nu = 1 \tag{2.7}$$

The term $g(\nu)$ is the laser lineshape in this case and when evaluated at ν, represents the fraction of the total number of photons found in the frequency interval of ν to $\nu + d\nu$.

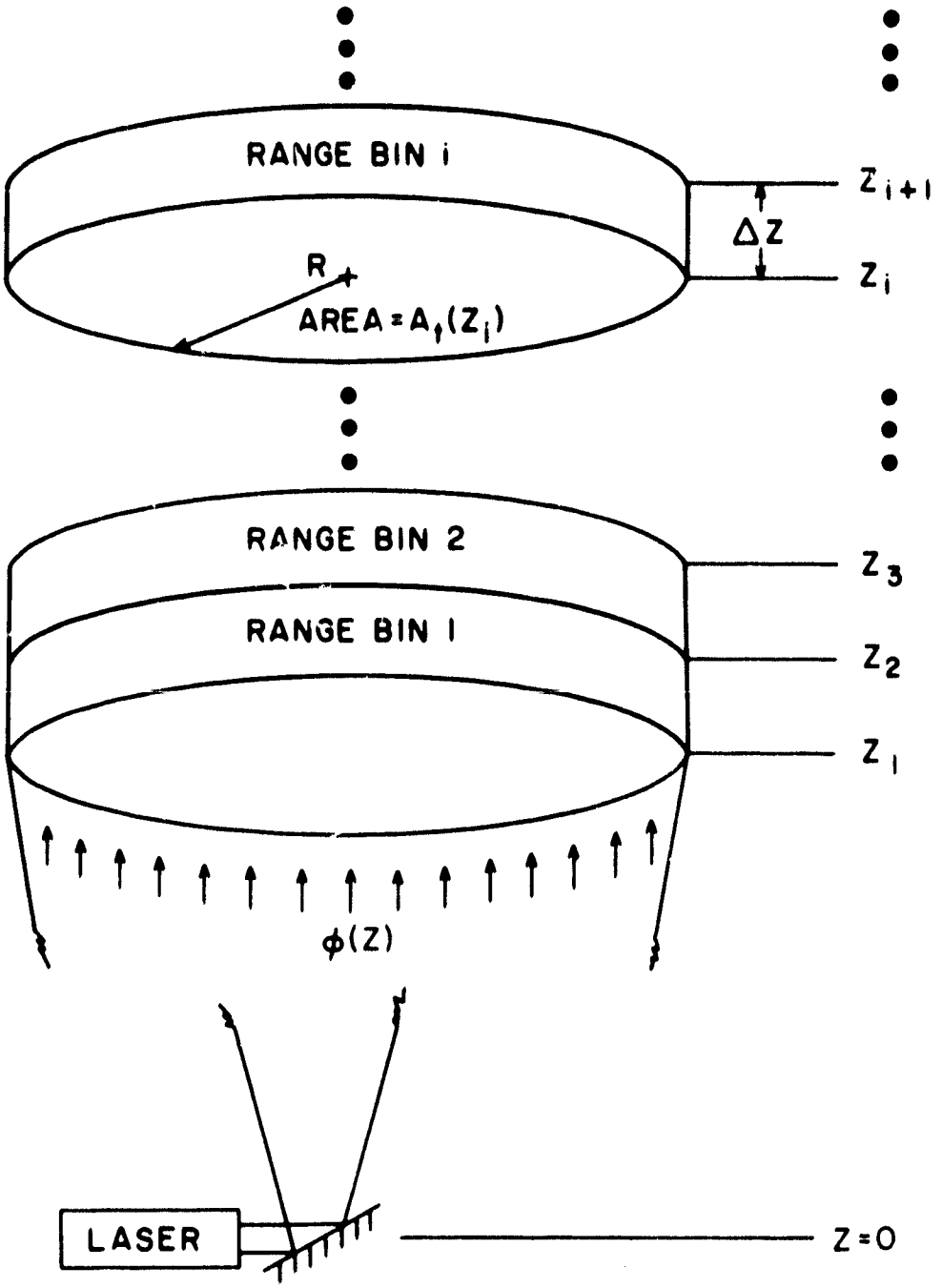

Figure 2.2 Diagram showing the transmitted light's geometry, including several range bins at different heights.

To write equation (2.1), it was assumed the laser pulse can be approximated by an impulse function. That is, all of the photons in the laser pulse are assumed to be at the same altitude and impinge on the bottomside of range bin i together. In reality, this is not the case. A more rigorous development will show the total intensity received will be proportional to the two-fold convolution of the scattering medium's concentration with height, the pulse shape of the laser in time, and the receiver gating function. The receiver gating function describes how the photons are sampled. For the Urbana lidar, this is a square pulse having a value of 1 during the time between samples and zero otherwise. As is the case with a convolution, the gating function and laser pulse shape will tend to obscure resolution in the concentration profile by smearing out the profile's fine structure. This process of obscuring fine structure as well as a development of the two-fold convolution can be found in *Richter and Sechrist* [1978].

Fortunately, through the use of digital signal processing means are available to reduce the effects of this convolution. *Rowlett and Gardner* [1979] discuss a technique for filtering the received signal with digital deconvolution filters. This work has proven quite successful in recovering the sodium concentration profile. Since the effects of a finite width pulse and gating function are mostly removed by this process, they will be neglected in this derivation.

For the resonance scattering process an absorption and spontaneous emission are required by each scattering atom. If the atom is collisionally deactivated, it will not add to the scattering process. Also, if the decay rate of the atom is too slow the range calculation will become more involved. For the case of the sodium layer, neither of these processes are important. The reason for this is that the decay time for the D_2 transition is 16 nsec which is much smaller than the sampling time of 3 μsec. This time is also much smaller than the average period between collisions at these altitudes which is between 1 to 100 μsec. Therefore, there is a negligible probability of the atoms either taking so long to decay that the resolution of the system is impaired or that the atoms will be collisionally deactivated.

An expression can now be developed to predict the number of photons collected by the receiving system. Figure 2.3 outlines the associated geometry

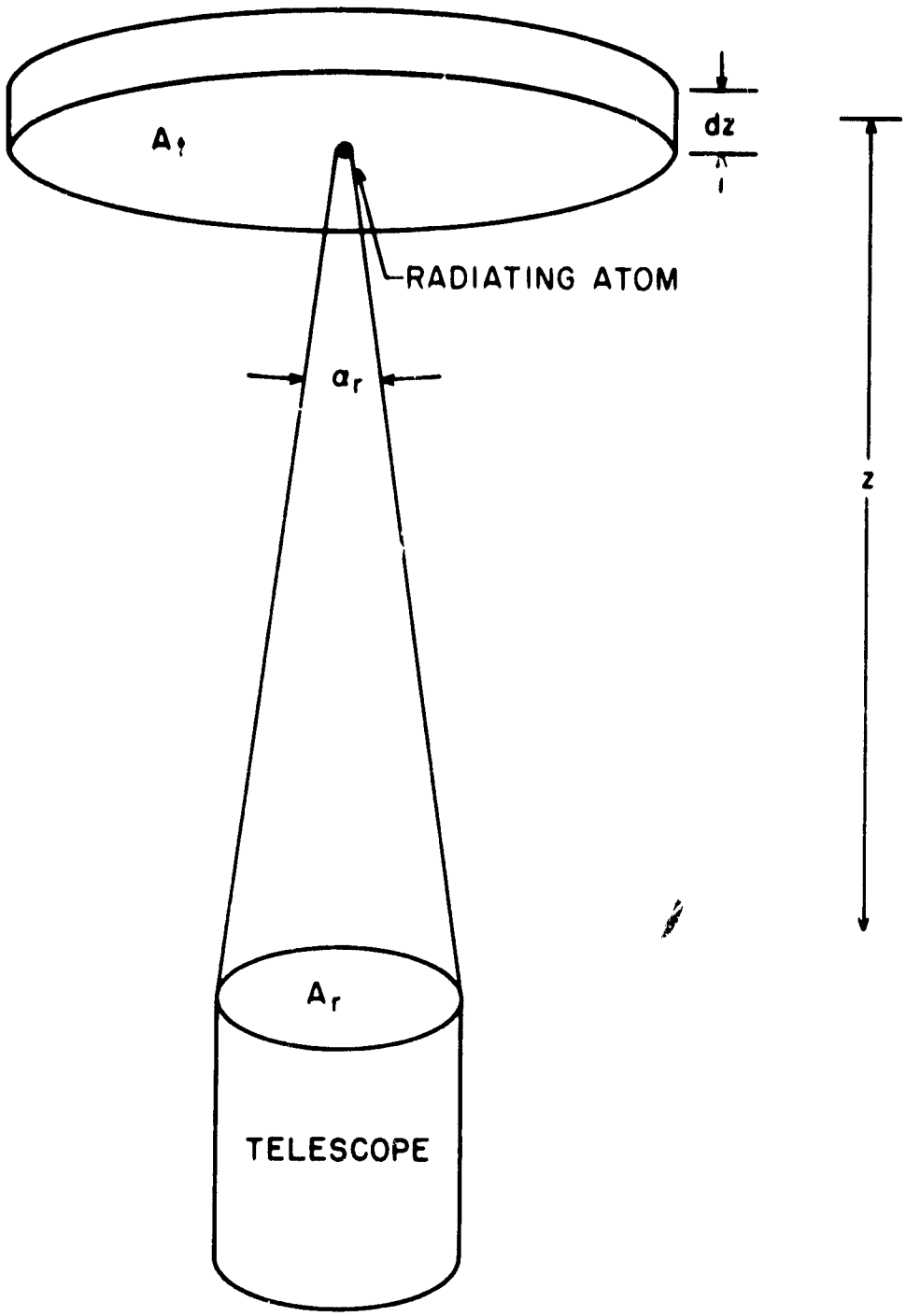

Figure 2.3 Geometry of the collection of photons from a cylinder of circular area A and thickness dz. The probability that light from one scatterer will be collected by the telescope in a lossless atmosphere is the solid angle the telescope subtends from the particle divided by 4π steradians.

for this collection process. Recalling the definition of the argular scattering cross section, the number of photons per frequency interval scattered by one sodium atom into a unit solid angle is given by:

$$N_{\beta,s}(\theta,\nu,z) = \sigma(\theta,\nu,z)\ \phi(\nu,z) \tag{2.8}$$

The θ dependence of $N_{\beta,s}$ can be removed by recalling that resonance scattering is isotropic. Therefore, $\sigma(\theta,\nu,z)$ can be replaced by the total scattering cross section divided by 4π steradians to obtain a unit solid angle basis. Equation (2.8) can now be rewritten as:

$$N_{\beta,s}(\nu,z) = \frac{\sigma(\nu,z)}{4\pi}\ \phi(\nu,z) \tag{2.9}$$

The number of sodium atoms in the differential volume shown in Figure 2.3 will be:

$$N_{Na}(z) = \rho(z)\,V(z) = \rho(z)A_t(z)\,dz \tag{2.10}$$

where $\rho(z)$ is the number density of sodium atoms at height z. It is assumed here that the laser divergence angle is small enough that the volume of the space which comprises the range bin can be approximated as a cylinder. The number of received photons can now be calculated as follows:

$$dN_p(\nu,z) = N_{Na}(z)\ N_{\beta,s}(\nu,z)\ \omega(z)\,T\eta \tag{2.11}$$

where ω is the solid angle subtended by the receiver aperture from a scattering atom, T is the atmospheric transmission back through the atmosphere to the receiver, and η is the receiver efficiency. The solid angle subtended by the receiver is given by:

$$\omega = \frac{A_p}{z^2} \tag{2.12}$$

The proper substitutions may now be made into equation (2.11) to obtain:

$$dN_p(\nu,z) = [\rho(z)\,A_t(z)\,dz] \times \left(\frac{\sigma(\nu,z)}{4\pi}\,\frac{N_t\,g(\nu)}{A_t(z)}\,T\right) \times \left(\frac{A_p}{z^2}\right) \times T \times \eta \tag{2.13}$$

Cancelling out $A_t(z)$ and rearranging yields:

$$dN_p(\nu,z) = \frac{N_t A_p T^2 \eta}{4\pi}\,\frac{\rho(z)}{z^2}\,g(\nu)\ \sigma(\nu,z)\,dz \tag{2.14}$$

Integrating each side over frequency in (2.14) removes the frequency dependence of dN_p and results in:

$$dV_r(z) = \frac{N_t A_r T^2 \eta}{4\pi} \frac{\rho(z)}{z^2} \left[\int_0^\infty g(\nu)\ \sigma(\nu,z) d\nu \right] dz \tag{2.15}$$

The term in brackets is defined as the effective cross section, σ_{eff}:

$$\sigma_{eff}(z) = \int_0^\infty g(\nu)\ \sigma(\nu,z) d\nu \tag{2.16}$$

The z dependence of σ_{eff} is due to temperature variations over altitude. For large enough linewidths, the temperature dependence is negligible and hence, so is the dependence on altitude. This approximation as well as other factors pertaining to the calculation of σ_{eff} are discussed in Section 2.4.

Finally, equation (2.15) can be integrated over the altitude interval of range bin i to obtain the number of photons one would expect to count from that range bin. Performing this integration produces the following expression:

$$N_i = \frac{N_t A_r T^2 \eta}{4\pi} \sigma_{eff} \int_{z_i}^{z_{i+1}} \frac{\rho(z)}{z^2} dz \tag{2.17}$$

Since the interval of integration is small, $\rho(z)$ can be approximated by the average concentration in range bin i, $\bar{\rho}_i$ and z can be approximated by the average altitude of range bin i, namely $(z_i + \Delta z/2)$. Sodium layers have shown scale heights as small as 2 km [*Gibson and Sandford*, 1971] which is still fairly large compared to the range bin thickness of 450 m. The range bin thickness is also only a small percentage of its altitude. Therefore, these approximations will result in very small errors. Upon making these approximations, the integration becomes trivial allowing equation (2.17) to be expressed as:

$$N_i = \frac{N_t A_r T^2 \eta\ \bar{\rho}_i\ \sigma_{eff}\ \Delta z}{4\pi (z_i + \Delta z/2)^2} \tag{2.18}$$

Recall that T is the transmission to the bottom of the layer. A value for it will be developed in Section 2.5.

2.4 *Effective Scattering Cross Section*

The effective scattering cross section as defined in equation (2.16) relates the scattering response to the frequency dependence of the atom as a scatterer combined with the frequency distribution of the light being used

for excitation. Essentially, equation (2.16) convolves the scattering cross section of the atom with the laser line shape.

The sodium resonance line shape is shown in Figure 2.4. Here, both the D_1 and D_2 lines are presented. Closer examination of the D_2 line shape shows that it is composed of two groups of three hyperfine lines. These groups are denoted as the D_{2a} and D_{2b} line for sodium. The D_{2a} line is located -2.14 m^{-1} from the line center position while the D_{2b} line is 3.56 m^{-1} away. Each of these lines is Doppler broadened and will have a linewidth given by:

$$\Delta\nu_D = \frac{2\sqrt{2R\ln 2}}{c}\,\nu_0\,\sqrt{\frac{T}{M}} \tag{2.19}$$

where: R = universal gas constant = 8.314 J/mole

c = speed of light

ν_0 = center frequency of the broadened line

T = temperature

M = molecular weight = 0.23 kg/mole.

Doppler broadening is described by a Gaussian line shape. Therefore, the scattering cross section for the entire D_2 line can be expressed as the sum of two properly weighted Gaussians. This weighting calculation was performed by *Richter and Sechrist* [1978] and results in a scattering cross section of:

$$\sigma(\nu) = \sigma_0\left\{\frac{20}{32}\exp-\left[\frac{(\nu-\nu_{Da})^2}{2\sigma_D^2}\right] + \frac{12}{32}\exp-\left[\frac{(\nu-\nu_{Db})^2}{2\sigma_D^2}\right]\right\} \tag{2.20}$$

Here σ_0 is the peak scattering cross section for the combined line and has a value of

$$\sigma_0 = \frac{1.66\times 10^{-6}}{\Delta\nu_D}\ m^{-2} \tag{2.21}$$

The terms ν_{Da} and ν_{Db} represent the center frequencies of the D_{2a} and D_{2b} lines, respectively. The variance of the two Gaussian expressions σ_D, is defined as:

$$\sigma_D^2 = \frac{\Delta\nu_D^2}{8\ln 2} \tag{2.22}$$

The lineshape of the laser can also be represented by a Gaussian of the form:

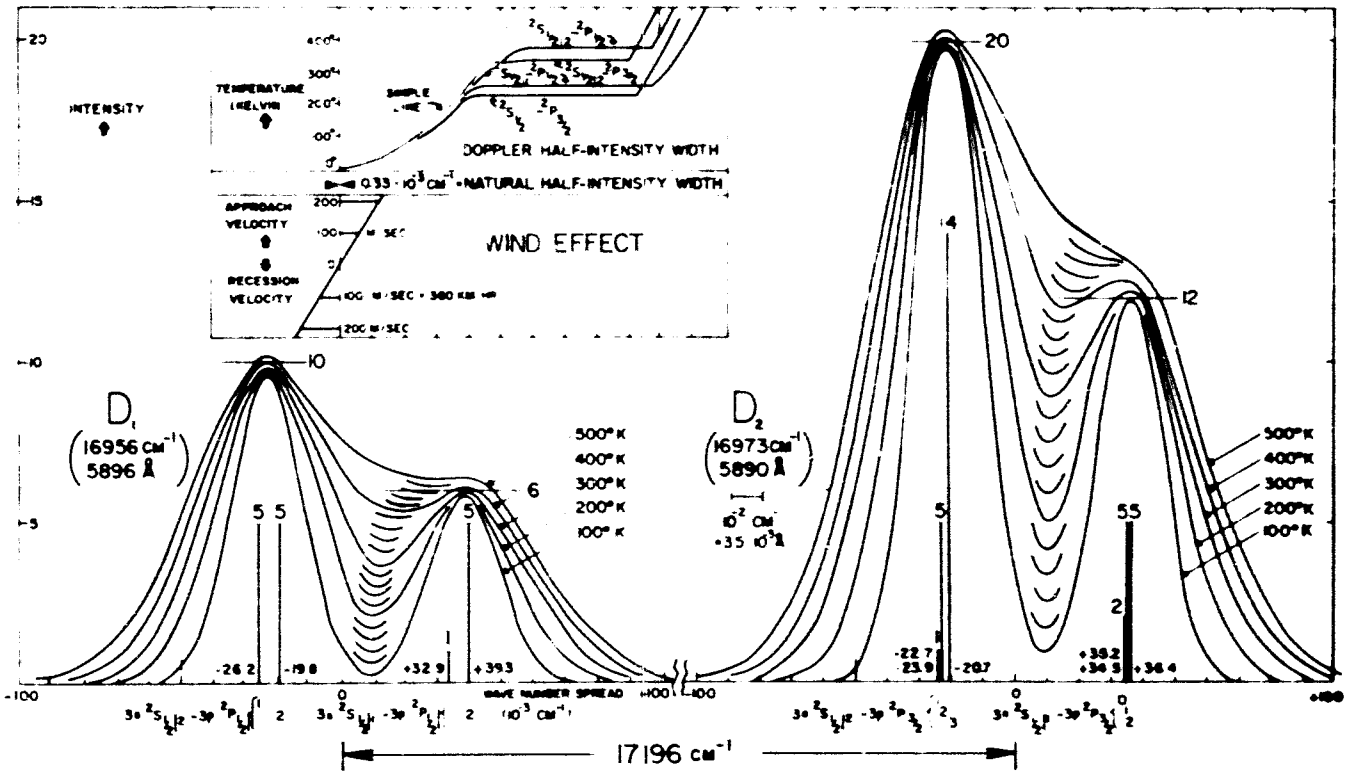

Figure 2.4 Line shape profile of the emission spectra from the sodium D_1 and D_2 lines for different temperatures. Note that the D_2 line is made up of two groups of three hyperfine lines. These groups are denoted as the D_{2a} and the D_{2b} line [Kuhn, 1961].

$$g(\nu) = \frac{1}{\sqrt{2\pi\ \sigma_L^{\,2}}} \exp - \left[\frac{(\nu - \nu_0)^2}{2\ \sigma_L^{\,2}}\right] \tag{2.23}$$

where $\sigma_L^{\,2} = \frac{\Delta\nu_L}{8\ \ln 2}$ = variance of the laser line

ν_0 = laser center frequency.

$\Delta\nu_L$ = laser linewidth.

Substituting equations (2.20) and (2.23) into equation (2.16) yields:

$$\sigma_{eff} = \int_0^{\infty} \frac{\sigma_0}{\sqrt{2\pi\ \sigma_L^{\,2}}} \exp - \left[\frac{(\nu - \nu_0)^2}{2\ \sigma_L^{\,2}}\right] \times$$

$$\left\{\frac{20}{32} \exp - \left[\frac{(\nu - \nu_{Da})^2}{2\ \sigma_D^{\,2}}\right] + \frac{12}{32} \exp - \left[\frac{(\nu - \nu_{Db})^2}{2\ \sigma_D^{\,2}}\right]\right\} d\nu \tag{2.24}$$

The lower limit of integration on equation (2.24) can be extended from 0 to $-\infty$ since there is a negligible contribution to the integral from this interval. That transforms the above integral into a convolution which has been solved by *Richter and Seehrer* [1978]. This new expression for σ_{eff} is then:

$$\sigma_{eff} = \frac{\Delta\nu_L\ \sigma_0}{\sqrt{\Delta\nu_D^{\,2} + \Delta\nu_L^{\,2}}} \times$$

$$\left\{\frac{20}{32} \exp - \left[\frac{4\ \ln 2(\nu_{Da} - \nu_0)^2}{\Delta\nu_D^{\,2} + \Delta\nu_L^{\,2}}\right] + \frac{12}{32} \exp - \left[\frac{4\ \ln 2(\nu_{Db} - \nu_0)^2}{\Delta\nu_D^{\,2} + \Delta\nu_L^{\,2}}\right]\right\} \tag{2.25}$$

Therefore, by knowing the temperature of the sodium as well as the linewidth and center frequency of the laser, the effective cross section may be calculated. Figure 2.5 shows how σ_{eff} depends on the linewidth for two values of the laser center frequency for sodium at a temperature of 200 K. The dip in σ_{eff} for lasers tuned to line center for small linewidths corresponds to the dip in the D_2 line at line center as observed in Figure 2.4. Clearly for small linewidths, tuning becomes very critical to obtain maximum values of σ_{eff}.

The previous section made the assumption that σ_{eff} did not vary over altitude. The validity of that assumption may now be investigated. Figure

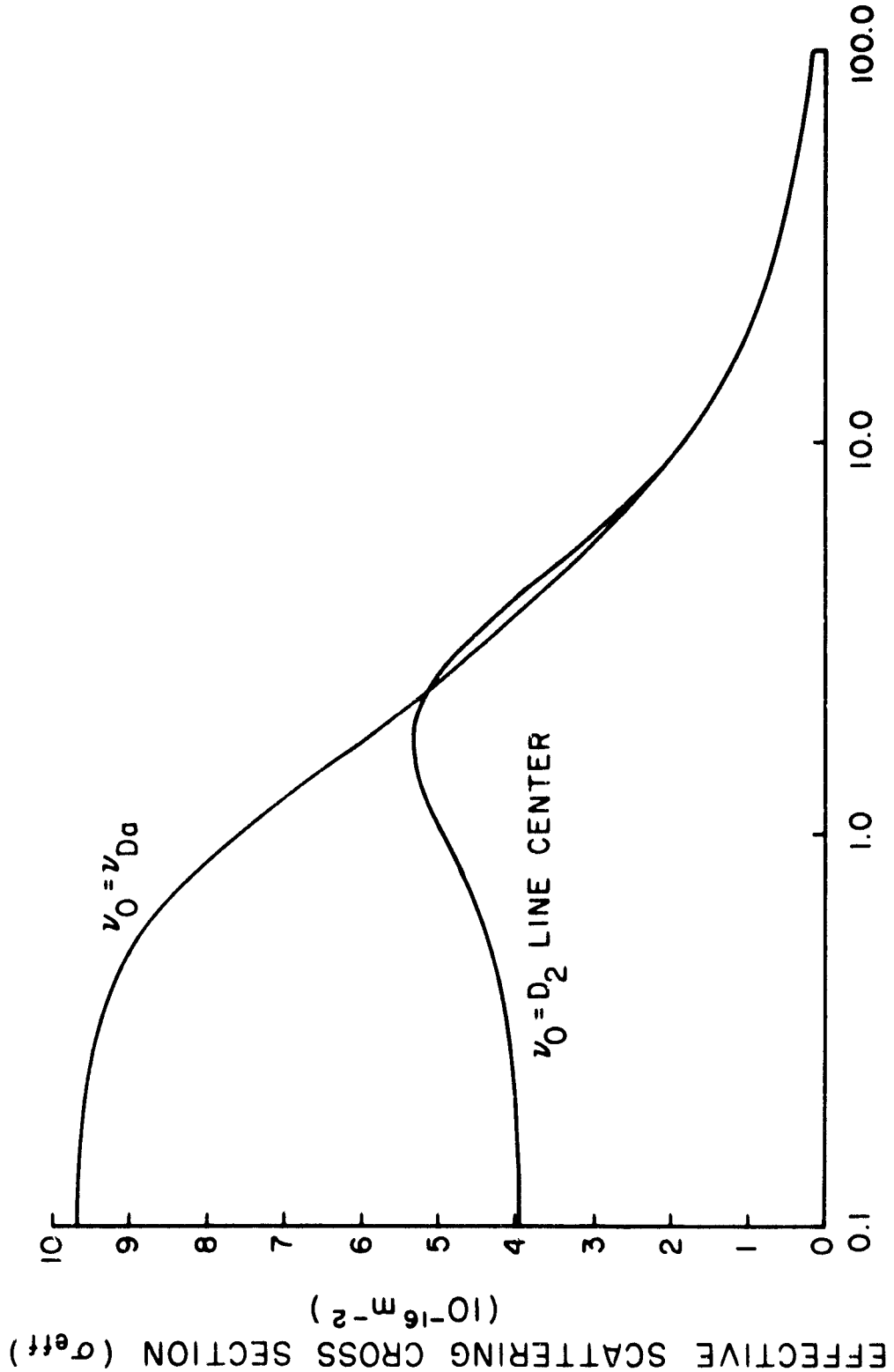

Figure 2.5 Plot of the effective cross section versus linewidth for laser center frequencies at line center and at the D_{2a} line position. The dip in the line center value is due to the dip in the sodium emission spectra.

2.6 shows the temperature dependence of σ_{eff} for linewidths of 0.1, 1 and 10 pm for lasers tuned to line center. A glance back at Figure 2.4 shows that the cross section figure is much more sensitive to temperature here than anywhere else. At midlatitudes, temperatures can vary from 170 K to 220 K over the altitudes where sodium is found [*U.S. Standard Atmosphere*, 1976]. For a large linewidth such as 10 pm, little if any variation can be observed over this temperature interval. Even for linewidths as small as 0.1 pm, a variation of around ±10% from the 200 K figure is evident. Therefore, it seems that assuming σ_{eff} to be constant over altitude is quite reasonable.

One last approximation can be made to equation (2.25) for large linewidths. $\Delta\nu_L$ dominates $\Delta\nu_D$ allowing $\Delta\nu_D$ to be neglected in the linewidth sum terms. This results in:

$$\sigma_{eff} = \frac{1.66 \times 10^{-6}}{\Delta\nu_L} \times$$

$$\left\{ \frac{20}{32} \exp - \left[\frac{4 \ln 2 (\nu_{Da} - \nu_0)^2}{\Delta\nu_L^2} \right] + \frac{12}{32} \exp - \left[\frac{4 \ln 2 (\nu_{Db} - \nu_0)^2}{\Delta\nu_L^2} \right] \right\} \quad (2.26)$$

The Urbana dye laser has a linewidth of 6.5 pm which equates to 5.62×10^9 Hz while the Doppler broadened line has a width at 200 K of 1.07×10^9 Hz. Equation (2.26) yields a value less than 2% in error for σ_{eff} compared with the more accurate expression in equation (2.25). This implies that equation (2.26) can be used with good accuracy for the present dye laser configuration.

2.5 *Transmission Losses Through the Sodium Layer*

In Section 2.3 the entire losses incurred by the beam as it propagated from the ground to range bin i were lumped into one term, T. Consider breaking this transmission coefficient into two terms. One term denoted T_A represents losses through the atmosphere to the bottom of the sodium layer. The second term will account for the transmission through the sodium layer only and will be denoted as T_{Na}. The total transmission term can now be represented by:

$$T = T_A T_{Na} \quad (2.27)$$

Before computing a value for T_{Na}, first consider a beam's transmission through an arbitrary range bin, where both the sodium concentration $\bar{\rho}$ and the cross section $\sigma(\nu)$ are constant throughout the range bin thickness.

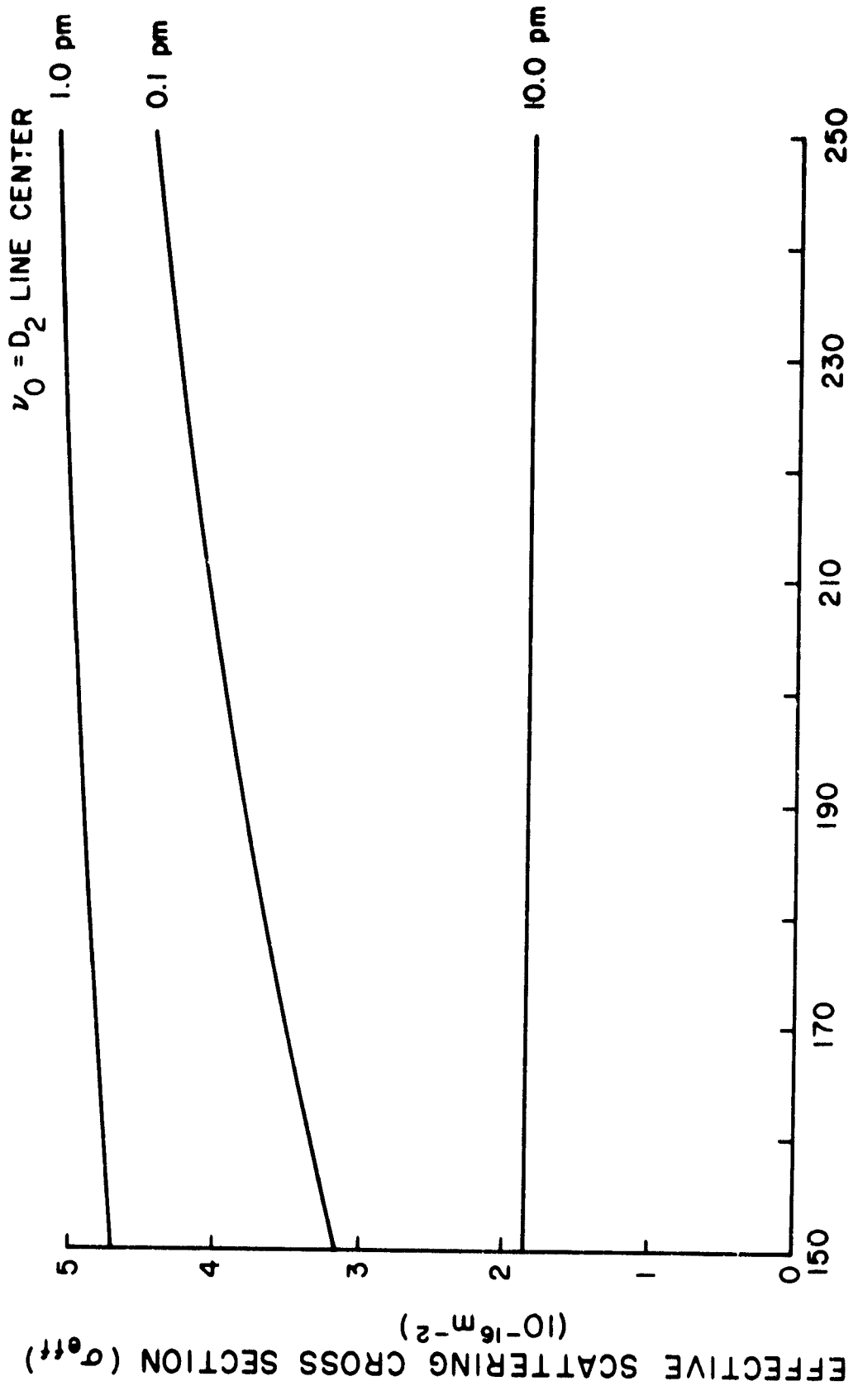

Figure 2.6 Plot of the effective cross section versus temperature for linewidths of 0.1, 1 and 10 pm tuned to line center. The 0.1 pm line shows the most sensitivity to changes in temperature corresponding to the increased sensitivity of the sodium emission spectra near line center.

For an impinging beam with a lineshape of $g(\nu)$, the number of photons absorbed by the layer in a frequency interval of ν to $\nu + d\nu$ can be expressed as:

$$N_a(\nu) = N_0\, g(\nu)[1 - T(\nu)] = N_0\, g(\nu)[1 - \exp(-\sigma(\nu)\,\bar{\rho}\Delta z)] \qquad (2.28)$$

where N_a is the number of absorbed photons per frequency interval and N_0 is the total number of photons at the bottom of the range bin of thickness Δz. The absorption is considered here due to its expression being easier to work with in succeeding steps. To obtain the total number of absorbed photons over all frequency, each side of equation (2.28) must be integrated over all frequency. This is done by first assuming that both $g(\nu)$ and $\sigma(\nu)$ can be expressed as Gaussians. The preceding section modeled $\sigma(\nu)$ as a sum of two Gaussians, however a single, equivalent Gaussian should provide accurate results for lineshapes with a linewidth equal to or greater than the P_2 complex width of 3 pm. Expressions for $g(\nu)$ and $\sigma(\nu)$ will then be given by:

$$\begin{aligned} g(\nu) &= G_0 e^{-\left(\frac{\omega}{\alpha}\right)^2} \\ \sigma(\nu) &= \sigma_0 e^{-\omega^2} \end{aligned} \qquad (2.29)$$

where: G_0 = linewidth normalization constant

σ_0 = maximum cross section value = $\sigma_{0a} + \sigma_{0b}$

$\omega = 2\sqrt{\ln 2}\,(\nu - \nu_0)/\Delta\nu_L$

$\alpha = \Delta\nu_L/\Delta\nu_D$.

This notation is somewhat different than that previously used, but will aid in subsequent steps.

Under these assumptions, an absorption coefficient, A can now be calculated in the following manner:

$$A = \frac{\int_{-\infty}^{\infty} N_a(\omega)\,d\omega}{\int_{-\infty}^{\infty} N_0 g(\omega)\,d\omega} \qquad (2.30)$$

The usual assumption concerning limit extension has been invoked here. This method of obtaining A is chosen to allow the integration to be carried out with respect to ω without having to go through the formality of a change in variables. Substituting (2.28) and (2.29) into equation (2.30) yields:

$$A = \frac{\int_{-\infty}^{\infty} \{1 - \exp[-\sigma_0 e^{-\omega^2} \bar{\rho}\Delta z]\} e^{-(\omega/\alpha)^2} d\omega}{\int_{-\infty}^{\infty} e^{-(\omega/\alpha)^2} d\omega} \tag{2.31}$$

This quotient has a series expansion [*Mitchell and Zemansky*, 1971] given by:

$$A = \frac{\sigma_0 \bar{\rho}\Delta z}{\sqrt{1+\alpha^2}} - \frac{(\sigma_0 \bar{\rho}\Delta z)^2}{2!\sqrt{1+2\alpha^2}} + \ldots + \frac{(-1)^n (\sigma_0 \bar{\rho}\Delta z)^n}{n!\sqrt{1+n\alpha^2}} + \ldots \tag{2.32}$$

Assuming values of $\sigma_0 = 1.66 \times 10^{-6}/\Delta\nu_p$ m^{-2}, $\bar{\rho} = 5 \times 10^9$ m^{-3}, $\Delta z = 450$ m, $\Delta\nu_L = 5.62 \times 10^9$ Hz ($\Delta\lambda_L = 6.5$ pm), $\Delta\nu_p = 1.07 \times 10^9$ Hz ($T = 200$ K) yields values of 6.53×10^{-4} for the first term and 8.11×10^{-9} for the second term in the series. Clearly the first term will dominate the series allowing the higher order terms to be dropped from equation (2.32) without much loss of accuracy. A value for the transmission through one range bin can now be expressed as:

$$1 - A = 1 - \frac{\sigma_0 \bar{\rho}\Delta z}{[1 + (\Delta\nu_L/\Delta\nu_p)^2]^{\frac{1}{2}}}$$

Combining the effects of all bins below bin i, the transmission of the beam from the bottom of the layer to bin i will be given by:

$$T_{Na} = \prod_{j=0}^{i-1} \left(1 - \frac{\sigma_0 \bar{\rho}_j \Delta z}{[1 + (\Delta\nu_L/\Delta\nu_p)^2]^{\frac{1}{2}}}\right) \tag{2.34}$$

Equation (2.34) represents the transmission of the laser beam upwards through the sodium layer. The light that travels downwards does not originate from the laser, but from the atoms themselves. Therefore, the distribution in frequency of the downwards travelling light will be different, causing a different transmission factor to be in effect. Assuming the distribution of the downwards travelling light can be approximated by a Gaussian of linewidth $\Delta\nu_p$, equation (2.34) will still be in effect after replacing $\Delta\nu_L$ by $\Delta\nu_p$. The downwards transmission through the sodium layer can be expressed as:

$$T_j = \prod_{j=0}^{i-1} \left(1 - \frac{\sigma_0 \bar{\rho}_j \Delta z}{\sqrt{2}}\right) \tag{2.35}$$

The upwards transmission as given in equation (2.34) will now be denoted as T_u. Applying this terminology to equation (2.18) yields:

$$N_i = \frac{N_t A_r \eta \, \Delta z \, T_A^2 \, \sigma_{eff}}{4\pi (z_i + \Delta z/2)^2} T_u T_l \bar{\rho}_i \tag{2.36}$$

One might wonder if the detailed expressions for T_u and T_l are worth the effort to calculate. To determine their effects on the concentration calculation, a simulation was carried out. The count values were assumed to have a Gaussian distribution centered at 90 km given by:

$$N = N_0 e^{-\alpha^2 (z - 90)^2} \tag{2.37}$$

The terms N_0 and α^2 as well as a lumped value for all the constant terms in equation (2.36) were chosen to yield a concentration of 5×10^9 m^{-3} at 90 km and a total column abundance of 5×10^{13} m^{-2}. These assumptions resulted in the concentration having the following representation:

$$\bar{\rho}_i = 6.2 \times 10^5 \frac{(z_i + .225)^2}{T_u T_l} e^{-\frac{(z_i - 90)^2}{400}} \tag{2.38}$$

where z_i is given in kilometers and $\bar{\rho}_i$ in m^{-3}.

The results of the simulation are shown in Figure 2.7. The figure shows the full correction, for both upward and downward propagation, accounts for an increase in the peak concentration of 10%. Most of that contribution comes from the downward propagation correction as revealed by the figure. Therefore, it seems worthwhile to include the sodium layer transmission terms in the expression for the sodium concentration.

2.6 *Rayleigh Normalization Method of Calibration*

In the expression for the counts from range bin i as given in equation (2.36), there are some factors which have yet to be discussed. Two of these factors in particular may prove difficult to measure or calculate. Those factors are the atmospheric transmission, T_A, and the total number of photons, N_t. At present, a nightly value of T_A does not exist for the Urbana lidar. This term should vary considerably for the different nights of observation due to different levels of haze, aerosols, clouds and other components which cause attenuation of the laser beam. It straightforward to measure

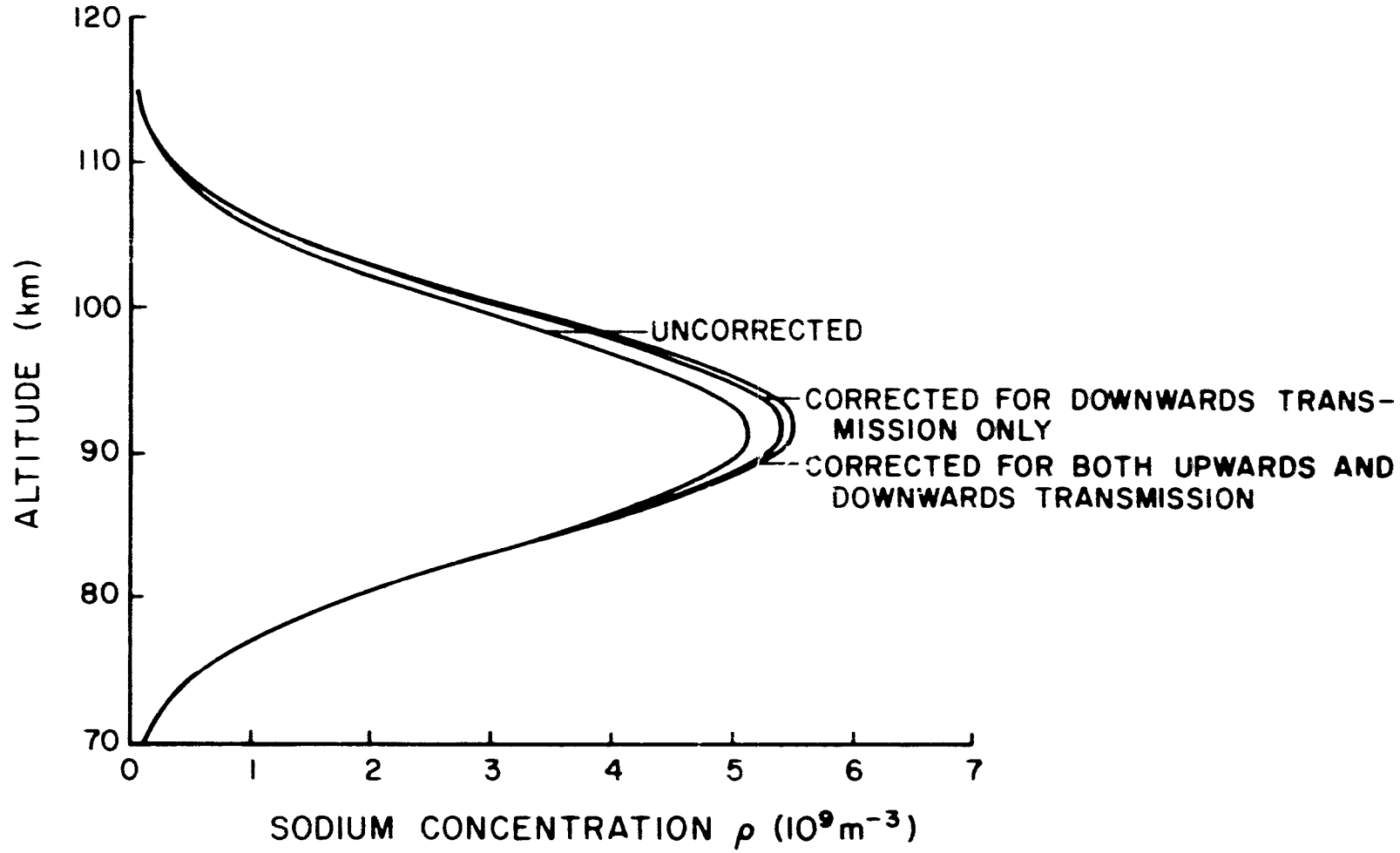

Figure 2.7 Simulation of the sodium layer to see the effect of including the laser transmission term. The inner curve has not been corrected, the middle curve corrected only for downwards transmission losses and the outer curve for two-way transmission.

the total number of photons. However, previous measurements have shown this figure to change on a shot to shot basis. Fortunately, a method exists which can eliminate both of these terms.

The elimination of difficult to evaluate terms is done by normalizing the returns from the sodium layer with returns from the Rayleigh region of the atmosphere. The returns from the Rayleigh region have been well studied and can be accurately predicted. To see how this normalization is carried out, an expression for the number of photocounts from the Rayleigh region must first be derived.

Consider a photon flux impinging on a range bin located in the Rayleigh scattering region of the atmosphere. The thickness of this bin is Δz and the center of the bin is located at an altitude z_R. Rayleigh scattering is not nearly as sensitive to frequency as resonance scattering. Therefore, the frequency dependence of the laser lineshape need not be taken into account. Under this assumption the photon flux can be expressed as:

$$\phi(z) = \frac{N_t}{A_t(z)} T_R \tag{2.39}$$

where T_R is the transmission to the bottom of the Rayleigh bin. The number of photons scattered by one air molecule per unit solid angle towards the telescope will be:

$$N_{s_R}(z) = \sigma_R(\theta,z)\ \phi(z) \tag{2.40}$$

The observation angle θ is π radians for this case since θ is measured from the initial direction of propagation. Backscattering is the term applied to this geometry. The number of scatterers in a differential volume will be:

$$n_R = \rho_R A_t(z)\, dz \tag{2.41}$$

These equations are combined in a manner similar to equation (2.11) to obtain a value for the number of photons counted by the system from the differential volume:

$$dN_p(z) = n_R(z)\ N_{s_R}(z)\ \Omega(z)\ T_R\ \eta \tag{2.42}$$

where η and Ω have the same definitions as given in Section 2.3. Making the proper substitutions, integrating over the altitude of the range bin, and making similar approximations to those made in Section 2.3 to evaluate the integral results in:

$$N_R = \frac{N_t A_r \eta \, T_R^2 \, \sigma_R(\pi) \, \Delta z}{z_R^2} \, \bar{\rho}_R \tag{2.43}$$

It was assumed that $\sigma_R(\pi)$ was constant over the range of integration. Next, dividing equation (2.36) by equation (2.43) and solving for $\bar{\rho}_i$ yields:

$$\bar{\rho}_i = \frac{4\pi (z_i + \Delta z/2)^2}{z_R^2} \frac{N_i}{N_R} \frac{T_R^2}{T_A^2 \, T_u \, T_d} \frac{\sigma_R(\pi)}{\sigma_{eff}} \bar{\rho}_R \tag{2.44}$$

It was shown by *Richter and Wehrli* [1978] that for values of z_R of 30 km or greater scattering and absorption losses to the beam from this altitude to the bottom of the sodium layer were about 1% in the absence of aerosols. Since significant amounts of aerosols rarely occur at this altitude, T_R and T_A may be equated without much loss of accuracy. It is common in sodium lidar work to incorporate the factor of 4π into the Rayleigh angular scattering cross section. Equation (2.44) may now be rewritten as:

$$\bar{\rho}_i = \frac{(z_i + \Delta z/2)^2}{z_R^2} \frac{N_i}{N_R} \frac{\sigma_R(\pi)}{\sigma_{eff}} \frac{\bar{\rho}_R}{T_u \, T_d} \tag{2.45}$$

This is the final form of the calibration equation. The next section discusses how a value for $\sigma_R(\pi)$ is obtained. Chapter 4 will discuss how an altitude, z_R, is chosen which will provide good results.

2.7 Rayleigh Scattering Cross Section

To derive an expression for the angular scattering cross section, first consider the volume total coefficient β. Recall that β represents the amount of energy scattered in all directions by a unit volume of scatterers. An expression for it is given as [*McCartney*, 1976]:

$$\beta = \frac{8\pi^3 (n^2 - 1)^2}{3\rho_N \lambda^4} \frac{6 + 3\rho_n}{6 - 7\rho_n} \tag{2.46}$$

where n and ρ_N are the index of refraction for the scattering media and ρ_n is a constant determined by the composition of the scatterer. The term in brackets is a depolarization factor due to molecular anisotropy with ρ_n having a value of 0.035 for air [*Penndorf*, 1957].

Next, the concept of phase function needs to be introduced. The phase function is defined as the ratio of energy scattered into a direction per

unit solid angle to the average energy scattered in all directions per unit solid angle. Under this definition the phase function $P(\theta)$ must satisfy the following condition:

$$\frac{1}{4\pi}\int_0^{4\pi} P(\theta)\, d\omega = 1 \tag{2.47}$$

where $d\omega$ is a differential solid angle. Anisotropy also affects the phase function. An anisotropy corrected $P(\theta)$ for air is given by *McCartney* [1976]:

$$P(\theta) = 0.7629\ (1 + 0.9324\ \cos^2\theta) \tag{2.48}$$

This phase function is for unpolarized light. Each of the components inside the brackets is for a particular component of polarized light. The 1 term is for light polarized in a direction perpendicular to the observation plane while the $\cos^2\theta$ term is for light polarized parallel to the observation plane. The observation plane is the plane which contains the line indicating the direction of travel for the incident light and the line in the direction of observation. For backscattering, each component contributes fairly equally, so that details concerning the polarization are not necessary for an accurate value of the phase function.

With the aid of the phase function, the angular volume scattering coefficient may be derived. Since the phase function represents the ratio of the energy scattered into one direction per steradian to the average energy scattered in all directions per steradian, the angular volume scattering coefficient may be found by multiplying $P(\theta)$ by the average energy scattered in all directions per steradian. This quantity is simply β divided by 4π steradians. Performing this multiplication results in:

$$\begin{aligned}\beta(\theta) &= \frac{\beta}{4\pi} P(\theta) \\ &= \frac{2\pi^2(n^2 - 1)^2}{3\rho_R \lambda^4} \frac{6 + 3p_n}{6 - 7p_n}\ 0.7629\ (1 + 0.9324\ \cos^2\theta)\end{aligned} \tag{2.49}$$

Recall that in Section 2.2, the angular scattering cross section could be found by dividing $\beta(\theta)$ by ρ_R. Remember also that the term $\sigma_R(\pi)$ as used in Section 2.6 included a factor of 4π. Performing these manipulations results in:

$$\sigma_R(\theta) = \frac{8\pi^3(n^2 - 1)^2}{3\rho_R^2 \lambda^4} \frac{6 + 3p_n}{6 - 7p_n}\ 0.7629\ (1 + 0.9324\ \cos^2\theta) \tag{2.50}$$

Penndorf [1957] has presented good tables by which $(n - 1)$ might be calculated. The $(n^2 - 1)^2$ term may be expressed in terms of $(n - 1)$ since n is so close to 1 for air. This approximation is given as:

$$(n^2 - 1)^2 \approx 4(n - 1)^2 \tag{2.51}$$

Since $\sigma_R(\theta)$ is only used for air and $\theta = \pi$, the depolarization factor and phase function may also be evaluated to combine with equation (2.51) to transform equation (2.50) into:

$$\sigma_R(\theta) = \frac{32\pi^3(n - 1)^2}{3\rho_R^2 \lambda^4} 1.53 \approx \frac{16\pi^3(n - 1)^2}{\rho_R^2 \lambda^4} \tag{2.52}$$

Another way also exists to calculate a value for $\sigma_R(\theta)$. *McClatchey and McGatt* [1978] gave an expression for β with corrections for frequency pressure and temperature as:

$$\beta = 9.807 \times 10^{-23} \left(\frac{273}{T}\right) \left(\frac{P}{1013}\right) \frac{1}{\lambda^{4.0117}} \tag{2.53}$$

where T is in Kelvin, P is in millibars and λ in centimeters. The units of β are inverse meters. The dependence on wavelength of $\lambda^{4.0117}$ instead of λ^4 is due to $(n - 1)$ having a slight dependence on wavelength. Following the procedure used earlier in the section, $\sigma_R(\pi)$ can be calculated by β in the following manner:

$$\sigma_R(\pi) = \frac{4\pi}{\rho_R} \frac{\beta}{4\pi} P(\pi) = \frac{\beta}{\rho_R} 1.4379 \tag{2.54}$$

Substituting equation (2.53) into the expression results in:

$$\sigma_R(\pi) = 1.41 \times 10^{-22} \left(\frac{273}{T}\right) \left(\frac{P}{1013}\right) \frac{1}{\rho_R \lambda^{4.0117}} \tag{2.55}$$

Figure 2.8 illustrates the change in $\sigma_R(\pi)$ over an altitude range of 25 to 50 km. Values for P, T and ρ_R were taken from the *U.S. Standard Atmosphere* [1976]. As can be seen, $\sigma_R(\pi)$ varies only 5% over the plotted altitude range. Deviations in the standard atmosphere parameters from the actual atmosphere are too great to make the variation of $\sigma_R(\pi)$ with altitude significant. Therefore, $\sigma_R(\pi)$ as evaluated at 35 km will be the value used in this study:

$$\sigma_R(\pi) = 4.75 \times 10^{-31} \text{ m}^{-2} \tag{2.56}$$

This value is between that reported by *Richter and Bechrist* [1978] and the value reported by *Measures* [1976], and can be assumed to incorporate the latest evidence available in the literature.

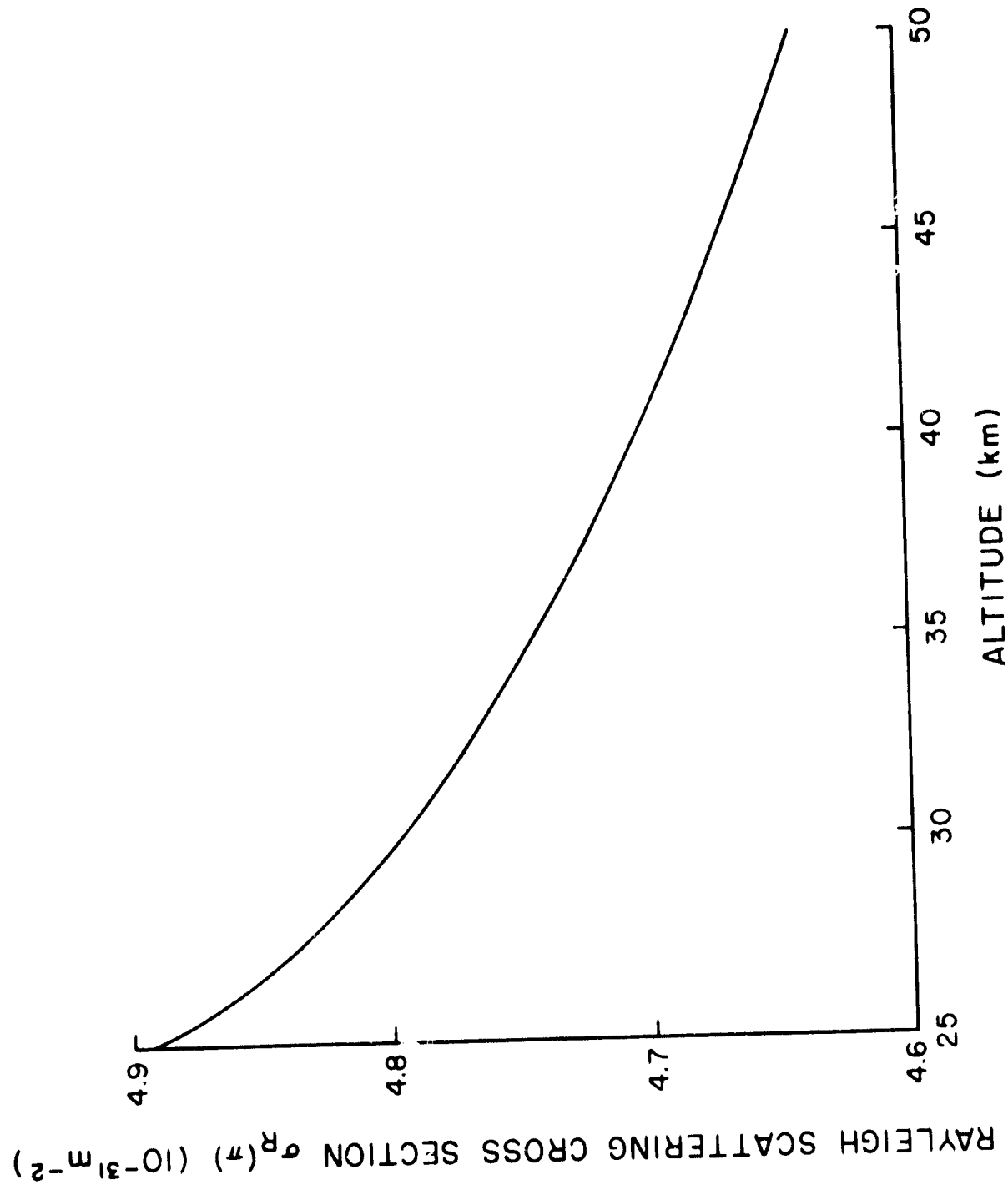

Figure [illegible] Plot of the variation of the Rayleigh scattering cross section versus altitude using atmospheric quantities taken from the [illegible] profile. Note the expanded scale on the vertical axis.

3. FABRY-PEROT FUNDAMENTALS AND USE IN MEASURING THE LINEWIDTH OF THE URBANA DYE LASER

3.1 *Introduction*

The previous chapter developed an expression for the effective scattering cross section, which is reproduced here:

$$\sigma_{eff} = \frac{1.66 \times 10^{-6}}{\Delta\nu_L} \left\{ \frac{20}{32} \exp - \left[\frac{4 \ln 2 (\nu_{Da} - \nu_0)^2}{\Delta\nu_L^2} \right] + \frac{12}{32} \exp - \left[\frac{4 \ln 2 (\nu_{Db} - \nu_0)^2}{\Delta\nu_L^2} \right] \right\} \qquad (3.1)$$

The cross section is a function of only two parameters which can vary, the laser center frequency ν_0 and the laser linewidth $\Delta\nu_L$. Both of these quantities are in terms of frequency units but are related to wavelength units by $\lambda_0 = c/\nu_0$ and $\Delta\lambda_L = c\Delta\nu_0/\nu_0^2$. The wavelength units convention will be used throughout this chapter.

The Urbana lidar system uses a sodium resonance cell as described in *Richter and Schriat* [1978] to monitor the position of the center frequency. To briefly describe this, the laser beam is passed through a cell which contains amounts of sodium vapor. The cell is heated to a temperature of around 150 C to provide a large enough partial pressure to ensure good resonance scattering of the beam when it is at the proper wavelength. When the laser is "off line", the cross section of equation (3.1) is very low and the beam passes through the cell unattenuated. When λ_0 approaches line center of the sodium D_2 complex, the cross section increases and one is able to observe scattered light in the cell. Once the laser has been tuned "on line", it is monitored frequently through the night to ensure that it stays "on line". Drifting due to thermal fluctuations and other factors does occur, so that adjustment is required from time to time. This study will assume this method is sufficient to assure the laser frequency is at line center. Errors to this approximation will be discussed in Chapter 5.

The second quantity that could vary in equation (3.1) was the laser linewidth. This quantity will be the focus for the remainder of this chapter. Linewidth measurements are carried out with the aid of a spectrometer. Spectrometers come in a wide variety of types and operating principles. One type, the Fabry-Perot spectrometer, fits both the given wavelength

resolution and available equipment requirements. Section 3.2 will describe and present the theory behind the operation of a Fabry-Perot spectrometer. Section 3.3 will discuss the c .teria taken into consideration when designing an interferometer, while Section 3.4 reports the results of the linewidth investigation of the Urbana lidar transmitter.

3.2 *Fabry-Perot Theory and Principles*

Fabry-Perot instruments operate on the principle of multiple beam interference. Multiple beam interference is the process in which an incident beam undergoes many divisions in amplitude, each division experiencing a certain amount of phase shift. The divided beams are then recombined allowing them to interfere with each other and form a characteristic fringe pattern. Figure 3.1 diagrams the interferometer used in this study. The two interferometer mirrors are the key members of the apparatus, since this is where the beam division is performed. Plane mirrors were used in this case, but there are other mirror configurations, confocal for instance, which also work. To simplify the discussion, only the plane Fabry-Perot is considered.

Figure 3.2 shows a detailed view of the mirror surfaces and the ray geometry for one incident monochromatic beam. As the figure shows, a set of rays emerges from the mirrors, each successive ray having undergone a phase delay that will be called δ. The group of rays which forms the reflected light from the interferometer won't be analyzed since only the transmitted rays make up the information that is being used to deduce the laser linewidth. *Born and Wolf* [1959] provide a good analysis of these reflected rays. The delay, δ, is just the phase difference between ray 0 and ray 1 as ray 0 propagates from points a to b while ray 1 propagates from points a to c to d. The delay for ray 1, δ_1, is given by

$$\delta_1 = \frac{2\pi}{\lambda} \frac{2l}{\cos\theta} + 2\phi \tag{3.2}$$

where ϕ is the phase shift encountered at each reflecting surface. The phase shift for ray 0, δ_0 can be expressed as:

$$\delta_0 = \frac{2\pi}{\lambda} 2l \tan\theta \sin\theta = \frac{2\pi}{\lambda} \frac{2l \sin^2\theta}{\cos\theta} \tag{3.3}$$

Combining these, δ is written as:

$$\delta = \delta_1 - \delta_0 = \frac{2\pi}{\lambda} \frac{2l}{\cos\theta} (1 - \sin^2\theta) + 2\phi \tag{3.4}$$

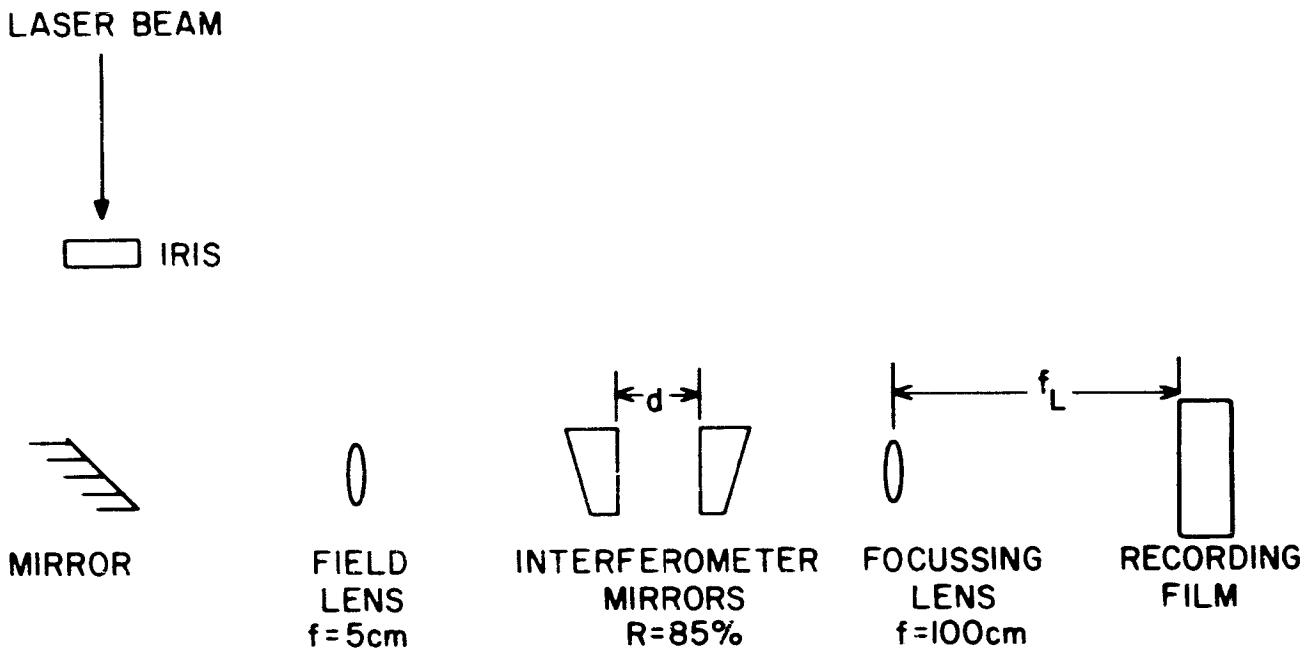

Figure 5.1 Block diagram of Fabry-Perot interferometer and support optics and equipment used to measure the linewidth of the Coherent dye laser.

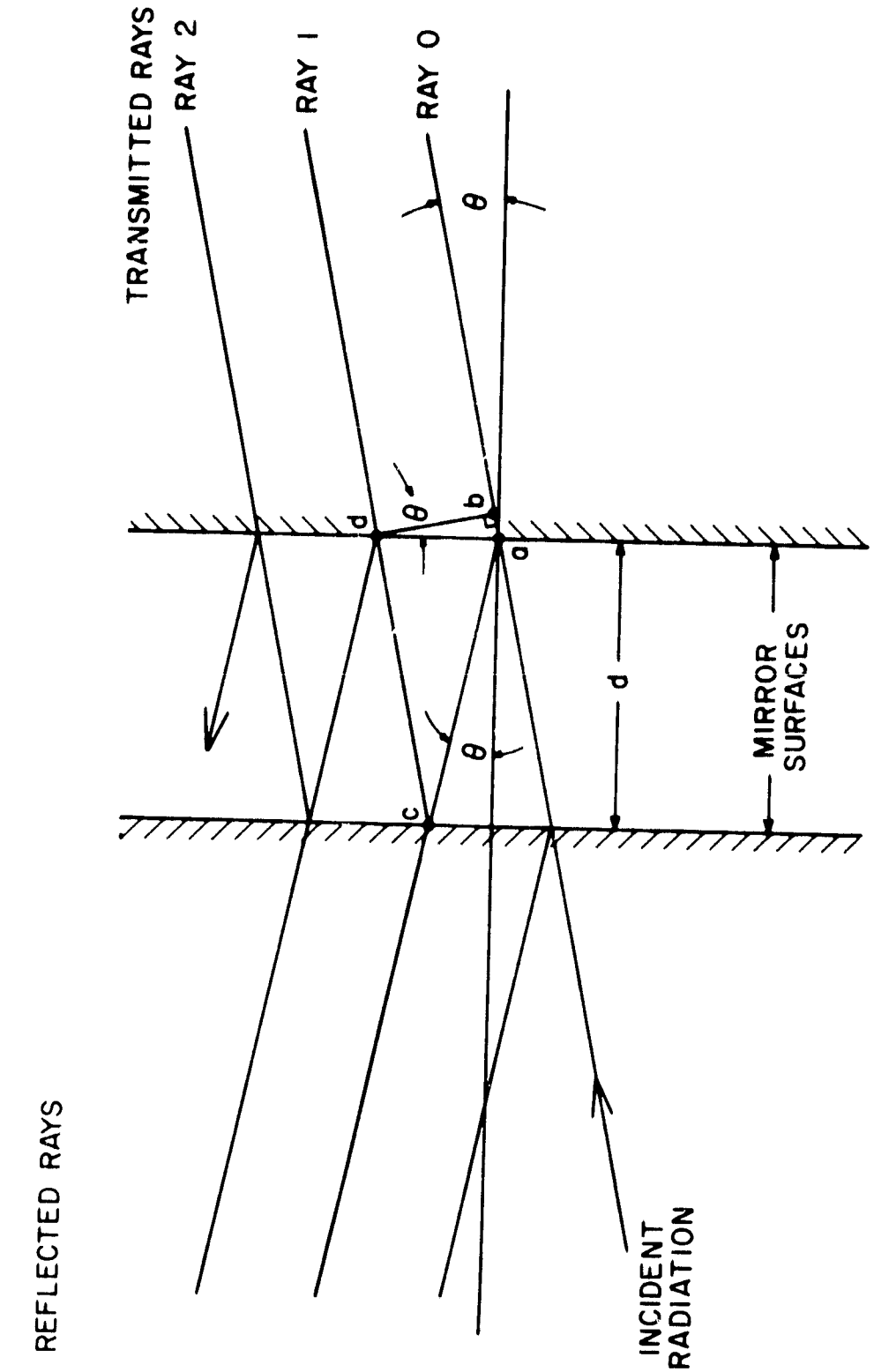

Figure 3.2 Diagram showing a closeup of the Fabry-Perot mirror surfaces and how the incident beam is multiply reflected.

which reduces to:

$$\delta = \frac{4\pi d}{\lambda}\cos\theta + 2\phi \tag{3.5}$$

An expression for the transmitted electric field can now be developed. Assume the mirrors are identical, each having a reflection coefficient of r and a transmission coefficient of t. Using common phasor notation, the electric field for ray 0 is given by:

$$E_0 = A_0 t^2 \tag{3.6}$$

where A_0 is the incident field strength amplitude and point b is taken as the zero phase reference. Ray 1's electric field can be written as:

$$E_1 = A_0 t^2 r^2 e^{-j\delta} \tag{3.7}$$

Generalizing the expression for ray n, we have

$$E_n = A_0 t^2 r^{2n} e^{-jn\delta} \tag{3.8}$$

The sum of all of these fields gives the total field expression:

$$E_T = \sum_{n=0}^{\infty} E_n = A_0 t^2 \sum_{n=0}^{\infty} (r^2 e^{-j\delta})^n \tag{3.9}$$

where it is assumed that an infinite number of beam divisions take place. Equation (3.9) is a geometric series and sums to:

$$E_T = \frac{A_0 t^2}{1 - r^2 e^{-j\delta}} \tag{3.10}$$

Since detection devices for light measure the light's intensity, the value for the transmitted intensity should be found:

$$I_T = E_T E_T^* = \frac{A_0^2 t^4}{1 - r^2(e^{j\delta} + e^{-j\delta}) + r^4} = \frac{A_0^2 t^4}{1 + r^4 - 2r^2\cos\delta} \tag{3.11}$$

If the incident intensity is denoted by $I_0 = A_0^2$ and the reflection and transmission coefficient are replaced by the reflectivity, $R = r^2$, and the transmissivity, $T = t^2$, (3.11) becomes

$$I_T = \frac{T^2 I_0}{1 + R^2 - 2R\cos\delta} \tag{3.12}$$

Equation (3.12) is one of the forms of the Airy function. The transmitted intensity pattern will be dependent on the plate reflectivity R and the

phase delay δ. δ itself is dependent on the beam's angle of incidence θ, the wavelength λ, mirror separation d and phase shift at the mirror's surface ϕ. Figure 3.3 shows a plot of the Airy function.

A closer look at δ is now in order, to see where constructive interference will occur. Looking at equation (3.12), I_r is clearly maximized when $\cos\delta$ is also a maximum, or when δ is a multiple of 2π. That condition can be stated as follows:

$$\delta = \frac{4\pi d}{\lambda}\cos\theta + 2\phi = 2q\pi \tag{3.13}$$

q being an integer. Next, incorporate the phase delay from the mirror reflection into q, making q generally a non-integer, that still increments by integers. This is done to simplify the ensuing manipulations and allows (3.13) to be rewritten as:

$$\delta = \frac{4\pi d}{\lambda}\cos\theta = 2q\pi \tag{3.14}$$

q is usually a very large number for common interferometer configurations. Assuming a mirror separation of 1 cm, a wavelength of 500 nm and small angles where $\cos\theta$ can be approximated as 1, q has a value of 4×10^5. Therefore, very small changes in either $\cos\theta$, d or λ will advance one to the $(q + 1)$th order of interference.

Figure 3.1 shows that the information recorded by the film in the interferometer is just the intensity variation as a function of θ. Figure 3.4 shows a plot of the Airy function where only θ is varying. This plot was made with $d = 5$ cm, $R = 0.85$ and $\lambda = 589$ nm. The condition on θ for intensity maxima is derived from equation (3.14) and is given as

$$2d\cos\theta = q\lambda \tag{3.15}$$

Note that q must decrease as θ increases, which means that intensity maxima which occur at larger angles are lower orders of interference. To see how the angle of incidence for constructive interference depends on the order of interference, let $q = q_0 - n$ where n is an integer ranging from 0 to infinity. Also, assume that $\frac{q_0\lambda}{2d} = 1$ so that the "zeroth" order of interference occurs along the optical axis, or at $\theta = 0$. Equation (3.14) can then be written as

$$\cos\theta_n = \frac{(q_0 - n)\lambda}{2d} = 1 - \frac{n\lambda}{2d} \tag{3.16}$$

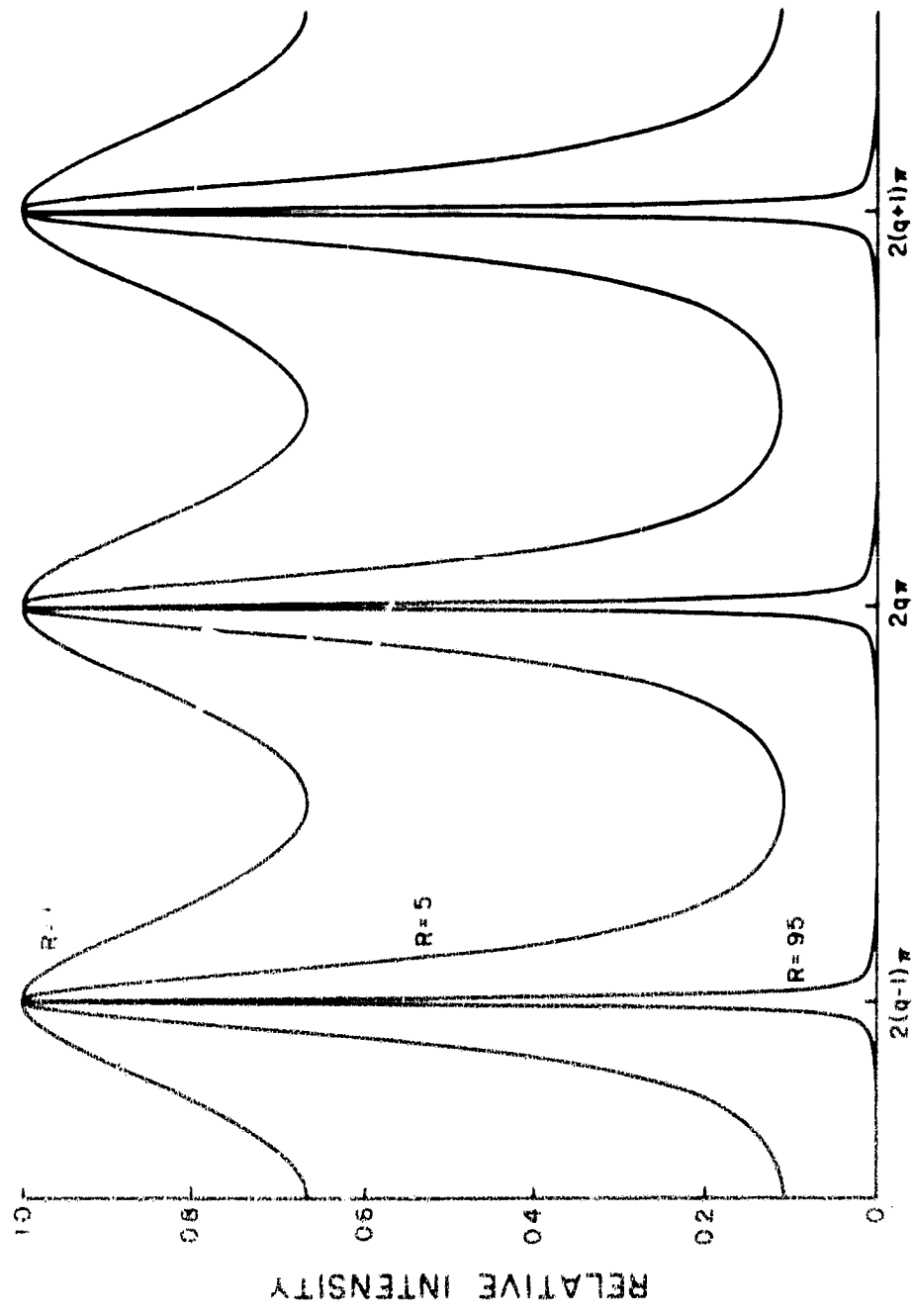

Figure 3.3 Plot of the transmission through a Fabry-Perot versus different values of δ for mirror reflectances of .10, .50, and .95. Note how the peak sharpens as R nears the value of 1.00.

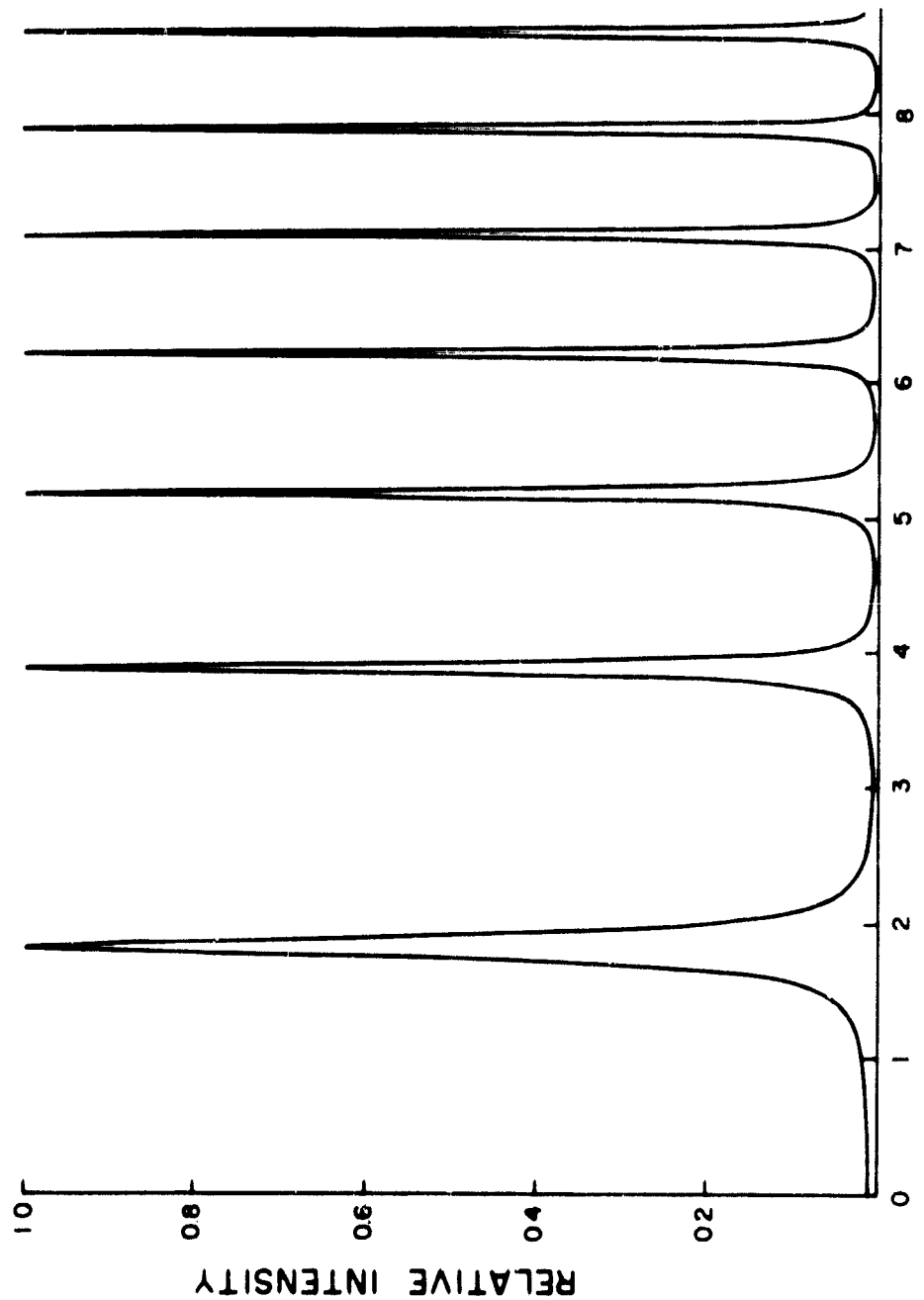

Figure 3.4 Plot of the transmission through a Fabry-Perot versus angle. Note that the transmission peaks tend to group together for larger angles.

Since θ_n will be small, $\cos\theta_n$ can be replaced by the first two terms in its series expansion,

$$1 - \frac{\theta_n^2}{2} = 1 - \frac{n\lambda}{2d} \tag{3.17}$$

Solving for θ_n then gives

$$\theta_n = \sqrt{\frac{n\lambda}{d}} \tag{3.18}$$

θ_n varies as the square root of the number of orders away from q_0. This is confirmed by Figure 3.4 which shows intensity maxima grouping closer together as higher angles are reached. Note also that as the mirror spacing d increases, θ_n decreases indicating that the intensity variation pattern will be pushed together for larger mirror separations.

The interference pattern that forms on the recording film will next be investigated. Figure 3.5 diagrams the back half of the interferometer. The divided beams leave the mirrors at an angle that will allow for constructive interference when recombined. The focusing lens provides the means of recombination by focusing the rays to a point in the lens' focal plane. There will also be light focused at other points where a ray is at an angle θ with respect to the optical axis. Therefore, the total two dimensional pattern recorded by the film will be the point rotated a full revolution around the optical axis, or in other words a ring pattern. This is shown in Figure 3.6 which is an actual photograph of the ring pattern produced by the dye laser light passing through the interferometer shown in Figure 3.1. The radius of the ring for a particular θ is easily found by looking at Figure 3.5 and is given by

$$\tan\theta = \frac{r}{f} \tag{3.19}$$

or, for small θ;

$$\theta = \frac{r}{f} \tag{3.20}$$

Throughout the discussion, only a monochromatic source of radiation has been considered. However, the purpose of this study is to measure the linewidth of the incident radiation which implies a continuum of monochromatic lines over a narrow wavelength region. Therefore, now consider two different wavelength components, one at λ, the other a small measure of

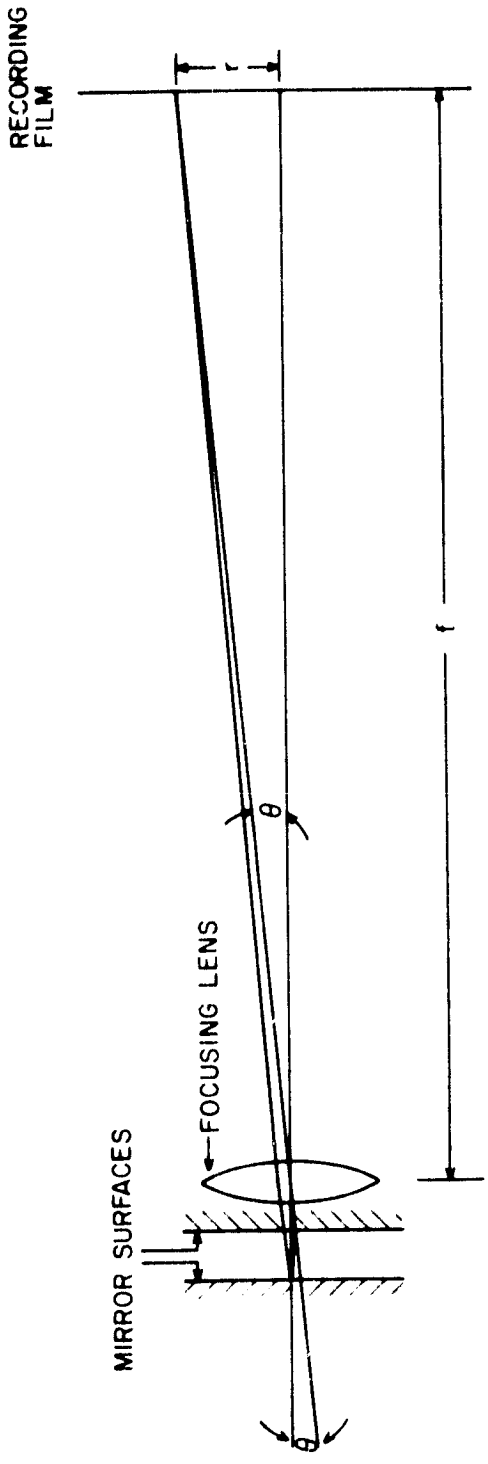

Figure 3.5 Diagram depicting the geometry of the focused parallel rays as they combine to form a ring pattern.

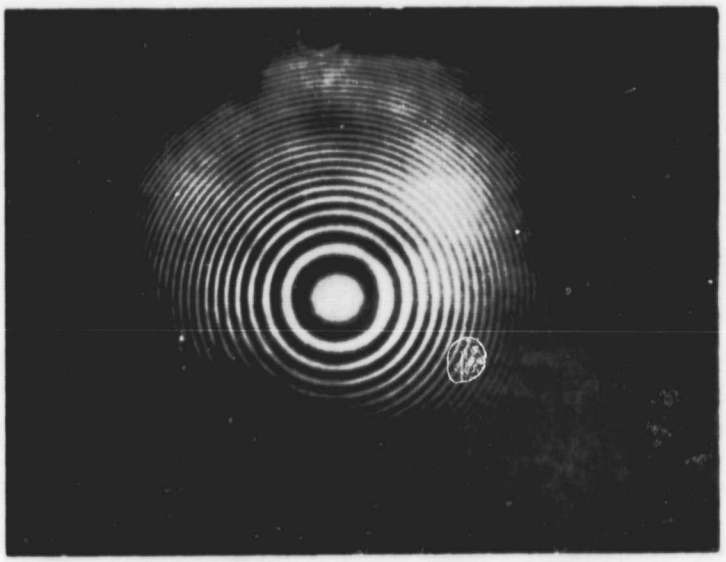

Figure 3.6 Photograph of the interference ring pattern of a laser pulse from the Urbana dye laser. The laser linewidth is proportional to the product of the ring's radius and thickness.

wavelength away at $\lambda - \Delta\lambda$. If the same order of interference is considered for both, say q, then the angle of incidence for the $\lambda - \Delta\lambda$ ray must be displaced from the λ ray to satisfy the condition for constructive interference, equation (3.14). Equation (3.14) can be written for each wavelength giving:

$$2d\cos\theta = q\lambda \tag{3.21a}$$

$$2d\cos(\theta + \Delta\theta) = q(\lambda - \Delta\lambda) \tag{3.21b}$$

where $\Delta\theta$ is the difference in angle needed to allow equation (3.14) to be satisfied at the different wavelength. Expanding the cos in equation (3.21b), it then becomes:

$$2d\cos\theta\cos\Delta\theta - \sin\theta\sin\Delta\theta = q\lambda - q\Delta\lambda \tag{3.22}$$

Several approximations are in order here. First both θ and especially $\Delta\theta$ are small enough that their cosine may be approximated by 1 and their sine by the angle itself. This allows (3.21) to be rewritten as:

$$2d = q\lambda \tag{3.23a}$$

$$2d - \theta\,\Delta\theta = q\lambda - q\Delta\lambda \tag{3.23b}$$

Solving (3.23a) for q and substituting into (3.22b) then yields:

$$\frac{\Delta\lambda}{\lambda} = \theta\,\Delta\theta \tag{3.24}$$

An expression for $\Delta\theta$ can be found by differentiating (3.20). Substituting this for $\Delta\theta$ and (3.20) itself for θ gives an expression for $\Delta\lambda$ in terms of measurable parameters r, Δr, f and λ of:

$$\Delta\lambda = \lambda\,\frac{r\,\Delta r}{f^2} \tag{3.25}$$

Δr represents the change in radius of the ring in going from λ to $\lambda - \Delta\lambda$.

An expression has now been developed which relates the quantity under study, the linewidth $\Delta\lambda$, of the laser output to the information that's recorded by the interferometer, namely the ring pattern. Next, information on the design of an interferometer that will give meaningful results is needed.

3.3 *Fabry-Perot Interferometer Design Criteria*

Re-examination of Figure 3.4 reveals that even for a monochromatic source, there is still a $\Delta\theta$ associated with the intensity peak. This $\Delta\theta$ would imply a corresponding Δr which in turn would indicate the source would have a finite linewidth of $\Delta\lambda$ as calculated by equation (3.24). This apparent $\Delta\lambda$ is due to the non-unity reflectance of the mirror set and indicates a minimum resolvable linewidth of the interferometer system. Figure 3.3

shows the way the peaks narrow as the reflectance goes up, however, even perfectly reflecting mirrors would not allow for an infinitesimally small resolvable bandwidth. This is due to the amount of light transmitted by the interferometer going down as the reflectance goes up. Clearly in the limiting case of unity reflectance, there will be no light transmitted and hence no pattern to record and measure. As it turns out, there are factors other than the mirror reflectance which cause broadening in the intensity peaks. Therefore, one cannot get arbitrary resolution by choosing high reflectances and detectors sensitive enough to record the associated reduced intensity. The factor which plays an important role in determining the minimum resolvable linewidth is the mirror flatness. This topic will be discussed later, but first consider only the effects of the mirror reflectivity.

Figure 3.7 shows a plot of the Airy function, equation (3.12), as a function of the phase difference δ. If only the wavelength is allowed to vary in the expression for δ, which is given in equation (3.14), then the plot becomes a function of wavelength. As the plot shows, the Airy function is quasi-periodic in wavelength, with a period that is called the free spectral range (FSR) of the interferometer. This is an important design parameter for interferometers and an expression will now be derived for it.

First write the condition for peak intensity, equation (3.15) for the qth order and the $(q - 1)$th order of interference:

$$2l \cos\theta = q\lambda \tag{3.26a}$$

$$2l \cos\theta = (q - 1)\ (\lambda + \Delta\lambda_{FSR}) \tag{3.26b}$$

where $\Delta\lambda_{FSR}$ is the change in wavelength necessary to compensate for the change in order. $\Delta\lambda_{FSR}$ is the free spectral range of the interferometer. To simplify the derivation assume the ring pattern is observed at a small angle, allowing $\cos\theta$ to be replaced by one. Subtracting equation (3.26a) from (3.26b) gives, after some rearrangement:

$$\lambda = (q - 1)\ \Delta\lambda_{FSR} \tag{3.27}$$

The small angle approximation allows equation (3.26a) to be solved for q giving

$$q = 2l/\lambda \tag{3.28}$$

q is going to be a very large number, as discussed earlier, allowing $(q - 1)$

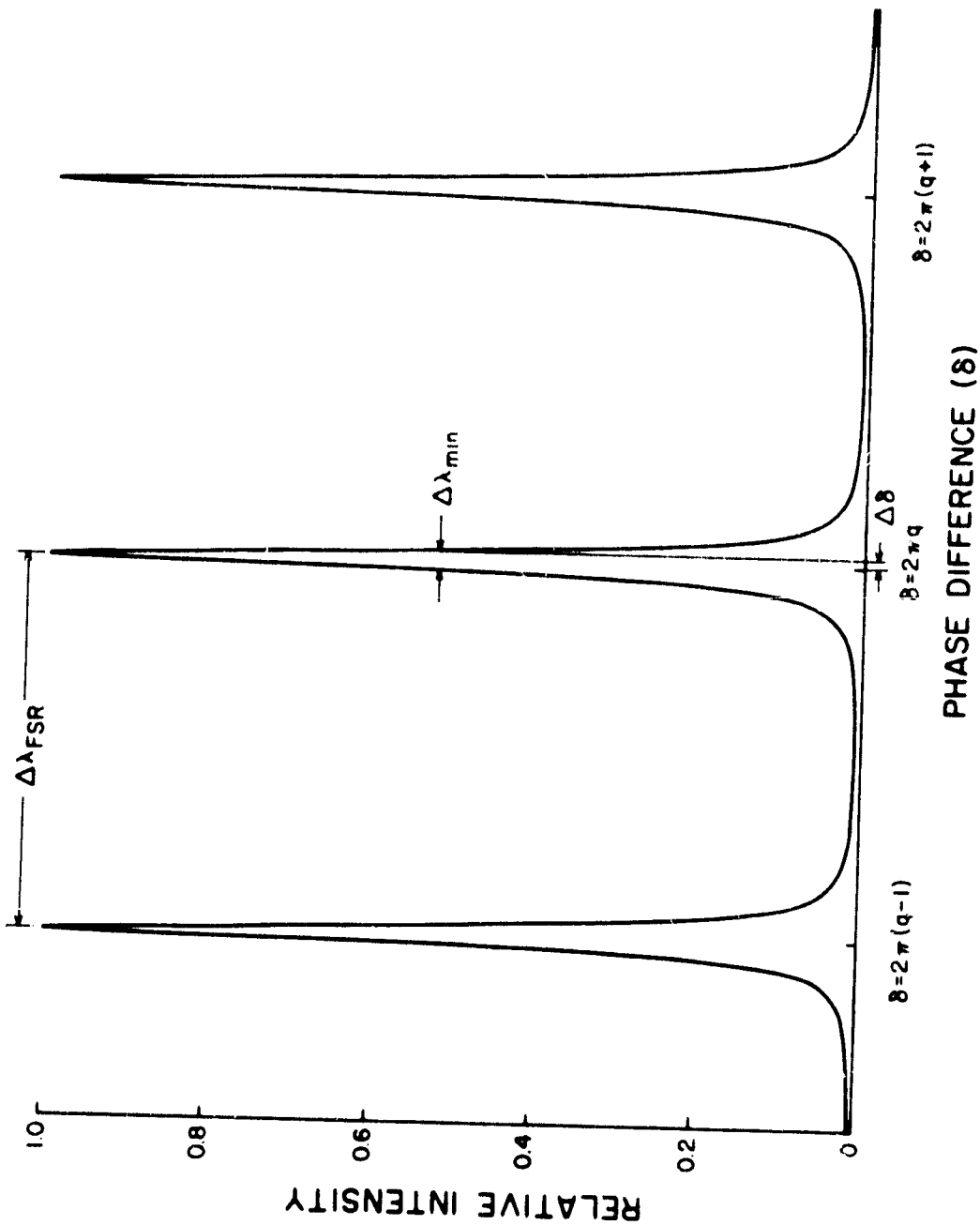

Figure 3.7 Plot of the transmission through a Fabry-Perot versus phase difference δ. Important quantities concerning Fabry-Perots are marked on the curve such as the free spectral range and minimum resolvable bandwidth.

to be replaced by q in equation (3.27). Incorporating both of these observations into equation (3.27) allows for the free spectral range to be solved in terms of measurable quantities:

$$\Delta\lambda_{FSR} = \lambda^2/2d \tag{3.29}$$

Note that as the mirror separation is increased, the FSR becomes smaller.

With this background, an expression for the minimum resolvable bandwidth of a system can be determined. Let $\Delta\delta$ be the phase difference necessary to move from the maximum to the half maximum of the intensity plot. Writing the normalized Airy function at the half maximum point yields:

$$\frac{1}{2} = \frac{(1 - F)^2}{1 + F^2 - 2F\cos(\delta_0 + \Delta\delta)} \tag{3.30}$$

where $\delta_0 = 2q\pi$. Rearranging and cancelling common terms transforms (3.30) to

$$2F\cos(\delta_0 + \Delta\delta) = 4F - 1 - F^2 \tag{3.31}$$

Expanding $\cos(\delta_0 + \Delta\delta)$ and applying $\delta_0 = 2q\pi$ to the proper terms then gives:

$$2F\cos\Delta\delta = 4F - 1 - F^2 \tag{3.32}$$

Next, replace $\cos\Delta\delta$ by the first two terms in its series expansion

$$-2F\frac{(\Delta\delta)^2}{2} = 2F - 1 - F^2 \tag{3.33}$$

which reduces to:

$$\Delta\delta = \frac{1}{\sqrt{F}}(1 - F) \tag{3.34}$$

Now, if $\Delta\delta$ is caused only by a change in wavelength, it can be expressed by differentiating equation (3.14) with respect to λ giving:

$$|\Delta\delta| = \frac{4\pi d\cos\theta}{\lambda^2}\Delta\lambda_{\frac{1}{2}} \tag{3.35}$$

where $\Delta\lambda_{\frac{1}{2}}$ represents the change in wavelength corresponding to the change in phase $\Delta\delta$. This will only be half of the minimum resolvable bandwidth $\Delta\lambda_{min}$. Using this along with equations (3.34) and (3.35) allows the solution for the minimum resolvable bandwidth to be obtained:

$$\Delta\lambda_{min} = \frac{(1 - F)}{\sqrt{F}}\frac{\lambda^2}{2\pi d\cos\theta} \tag{3.36}$$

Making the small angle approximation and rearranging yields

$$\Delta\lambda_{min} = \frac{\lambda^2/2d}{\frac{\pi\sqrt{R}}{1 - R}} \tag{3.37}$$

The numerator of this expression is just the FSR of the interferometer. The denominator is called the finnese, F, where

$$F = \frac{\pi\sqrt{R}}{1 - R} \tag{3.38}$$

For a given FSR, a larger finesse will give the interferometer a smaller minimum resolvable bandwidth. Therefore, the finesse can be regarded as a figure of merit for the Fabry-Perot device. Note that as the reflectance goes to unity, the finesse goes to infinity.

This expression for the finesse was developed for perfectly flat mirrors with an arbitrary reflectivity. As mentioned before, a deviation from perfect flatness will cause the intensity peaks to broaden. The effect of this deviation from flatness can be expressed in terms of another finesse figure, the flatness finesse. Equation (3.38) then refers to the reflective finesse. For mirrors which deviate from parallelism by an amount λ/M, the flatness finesse will be given by

$$F_f = M/2 \tag{3.39}$$

For mirrors flat to $\lambda/50$, this would imply a flatness finesse of $F_F = 25$.

The total instrument finesse can now be calculated for real-life interferometers as

$$\frac{1}{F_m} = \left[\frac{1}{F_R^2} + \frac{1}{F_F^2} \right]^{1/2} \tag{3.40}$$

where F_m is the total instrument finesse and F_R is the reflective finesse, equation (3.38). Therefore, the part of the finesse which is lowest will tend to dominate the total finesse.

The interferometer design will be considered now. The two major design criteria are:

1) To choose a free spectral range which is larger than the expected linewidth of the light to be measured,
2) Given the free spectral range from above, to choose a finesse large enough to give a minimum resolvable bandwidth smaller than the expected linewidth.

If condition one is not met, the rings will be so wide that they will overlap orders and destroy the ring pattern. This is apparent after some thought about the meaning of the FSR. Condition two ensures that we are actually measuring the linewidth of the laser and not just the instrument bandwidth.

With an FSR chosen, using equation (3.29), the proper mirror spacing can be chosen. Next, with the minimum required finesse known, one can choose a set of mirrors that will have a large enough reflectance and sufficiently good flatness figure. In order for the mirrors to be aligned well enough to yield a high finesse, a mount that is very mechanically stable and is resistant to thermal fluctuations must be used. Commonly, some type of invar is used in this mount's construction to provide the thermal stability required. If the mount vibrates or expands over even small fractions of the light's wavelength, alignment suffers and the finesse is reduced.

A review of Figure 3.1 also shows values of two lens focal lengths to be chosen. The focusing lens focal length should be chosen large enough to make the ring pattern large enough to easily observe. Equation (3.25) shows that for a given $\Delta\lambda$ and λ; r and Δr must increase to offset increases in f, thus providing a larger and more observable ring pattern. The field lens focal length must be small enough to allow for a wide variety of incident angles so that plenty of orders of interference will be excited. If D is the laser beam diameter and f_F the field lens focal length, it is easily shown from equation (3.18) that the number of rings excited by the field lens is given by

$$N = \frac{D^2}{4 f_F^2 \lambda} \tag{3.41}$$

Under normal conditions, N is quite large and needn't be worried about.

3.4 *Experimental Design, Setup and Results*

Previous evidence indicated that the linewidth for the Urbana dye laser would be somewhere around 10 pm [*Molectron and Coherent*, 1978]. Therefore, using the design criteria discussed in the previous section, it was felt that an FSR of 15 pm would be appropriate for this study. This value for the FSR corresponds to a mirror separation of 1.16 cm. The next step was to find a set of mirrors which would provide a high enough finesse, when aligned properly, to provide the instrument with a low enough minimum

resolvable linewidth to perform the measurement. A set of 85 percent reflective mirrors which were flat to $\lambda/20$ were readily available. This set of mirrors has a reflective finesse of 19.3 and a flatness finesse of 10, yielding a total finesse, as calculated by equation (3.40), of 8.9. Using equation (3.37) for this finesse figure and the previously mentioned FSR of 15 pm, a minimum resolvable linewidth of 1.7 pm was calculated. This would work quite well for the estimated linewidth. These quantities and equipment specifications are listed in Table 3.1.

It was important to have a good mechanically and thermally stable mount which would hold the mirrors and allow them to be adjusted to an accurate degree of parallelism. Figure 3.8 exhibits a photograph of the mount used in this study. The spacing rods are constructed of steel, with the mounting plates manufactured at close tolerances to reduce slipage on the rods.

Again, Figure 3.1 diagrams the equipment setup. A description of the alignment procedure for this equipment now follows. Using the beam from the continuous wave HeNe alignment laser, the basic system equipment is put into place. This includes the iris, the folding mirror and the mount, without mirrors in place. The folding mirror is now adjusted so that the beam passes through the optical axis of the mirror mount. Next, the front mirror is put into place and it is adjusted so that the HeNe beam retroreflects back through the iris. The back mirror is then put into place. Some sort of dot pattern will most likely now appear on a viewing screen in back of the interferometer. This is the HeNe beam as it unstably walks off the mirrors. The back mirror is now adjusted to bring the dots closer together until they all fall on top of each other. This should be done with as much precision as possible. The field lens is next put into place, two to three focal lengths away from the front mirror surface and positioned so that the beam stays in the optical axis. This can be done by placing an iris stopped all the way down in the HeNe beam at the point where the field lens focus is expected to fall. Then the field lens is inserted and adjusted so that the focused spot falls in the center of the iris. This second iris can now be removed and the focusing lens put into place. Again, this lens should be placed so that its center falls onto the optical axis, although the adjustment is not so critical as for the field lens. A viewing screen is then placed one focal length away from the focusing lens. This distance should be measured with as much accuracy as possible to minimize

Table 3.1 Parameters and specifications of the Fabry-Perot interferometer used to measure the linewidth of the Urbana dye laser.

Equipment/Parameter	Value
Center Wavelength (λ)	589 nm
Reflectance (R)	.85
Flatness	$\lambda/20$
Spacing (d)	1.16 cm
Free Spectral Range ($\Delta\lambda_{FSR}$)	15 pm
Reflective Finesse (F_R)	19.3
Flatness Finesse (F_F)	10
Total Finesse (F_T)	8.9
Minimum Bandwidth ($\Delta\lambda_{min}$)	1.7 pm
Field Lens Focal Length (f_F)	5 cm
Focusing Lens Focal Length (f)	100 cm

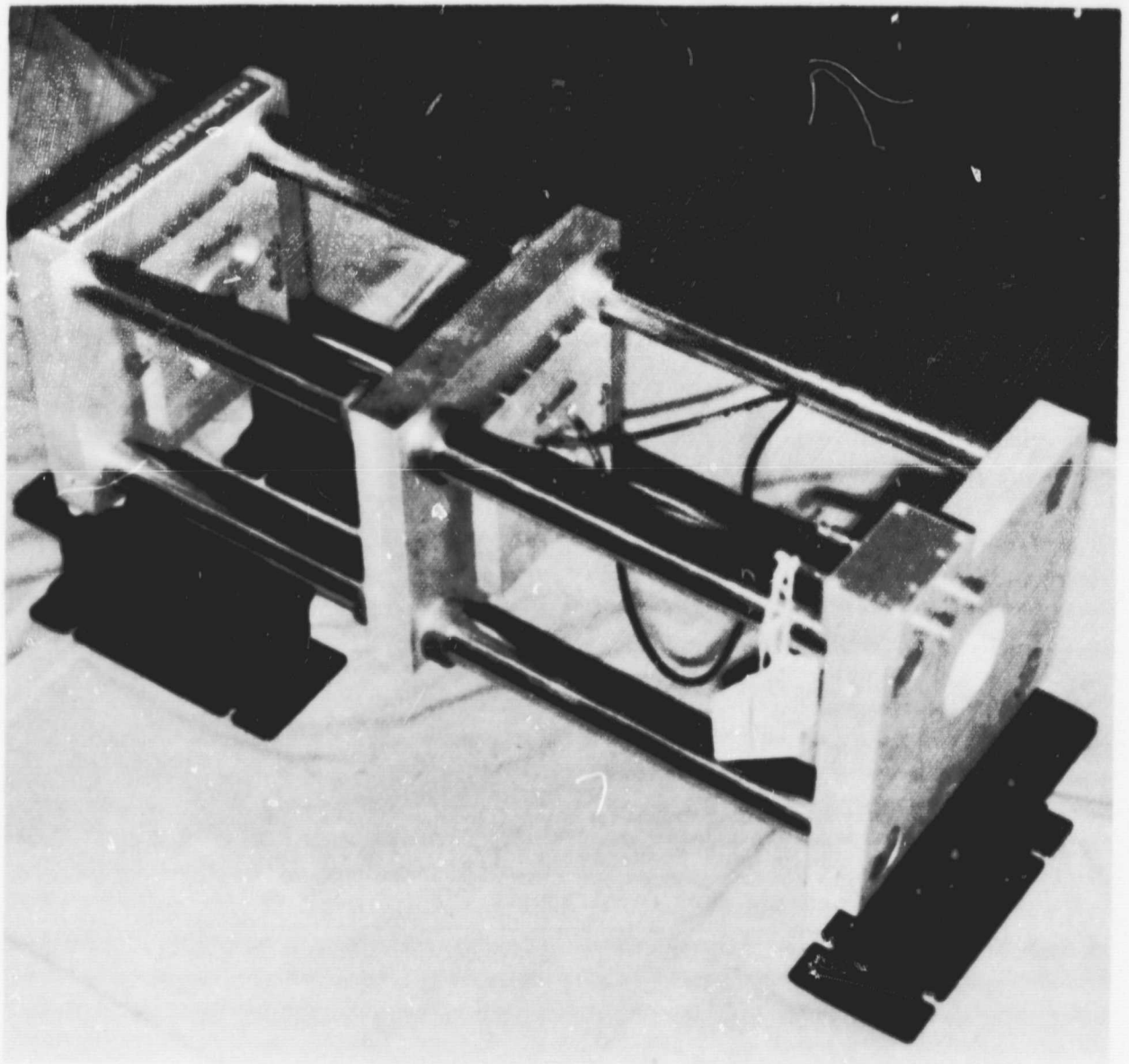

Figure 3.8 Photograph of the Fabry-Perot mirror mount. The front mirror of the interferometer is held on the left-hand plate with the back mirror located on the movable middle plate.

focusing error. A ring pattern should now be observable. If the pattern appears unsymmetric, small adjustments can be made on the back mirror in the interferometer set to allow for the best attainable ring pattern. The covered recording film can now be put into place. The position of the film should be in the focusing lens focal plane. The dye laser is then turned on at this point to ensure the ring pattern has good symmetry and is positioned properly with respect to the recording film. The apparatus, from the interferometer mount on back, should now be covered by a light tight cloth to prevent stray light from reaching the film. The apparatus, after alignment, was photographed and is shown in Figure 3.9.

To take a picture of the ring pattern, the beam to the interferometer is blocked off until the film has been uncovered. One laser shot is allowed to pass through and then the film is re-covered and developed. This study simply used the back end of an oscilloscope camera with type 40 Polaroid film, allowing quick viewing of the photograph. If the photograph has not received the correct exposure, the beam intensity must be adjusted. For over-exposures, the use of a less reflective mirror in sampling the beam or an interference filter placed in the beam work well in reducing the incident energy on the film. The interference filter is especially suitable since its transmission characteristics are a function of the beams angle of incidence to the surface. Therefore, by varying the angle of the filter with respect to the beam, a continuum of intensities can be produced.

Figure 3.7 shows a photograph properly exposed. A traveling microscope was used to record the position of several of the rings for various cross sections through the ring pattern. Values for p times Δp were determined for the rings sampled, through each cross section. These were averaged together and inserted into equation (3.25) along with f = 100 cm and λ = 589 nm. This yielded a calculated linewidth of 6.0 ± 2.5 pm.

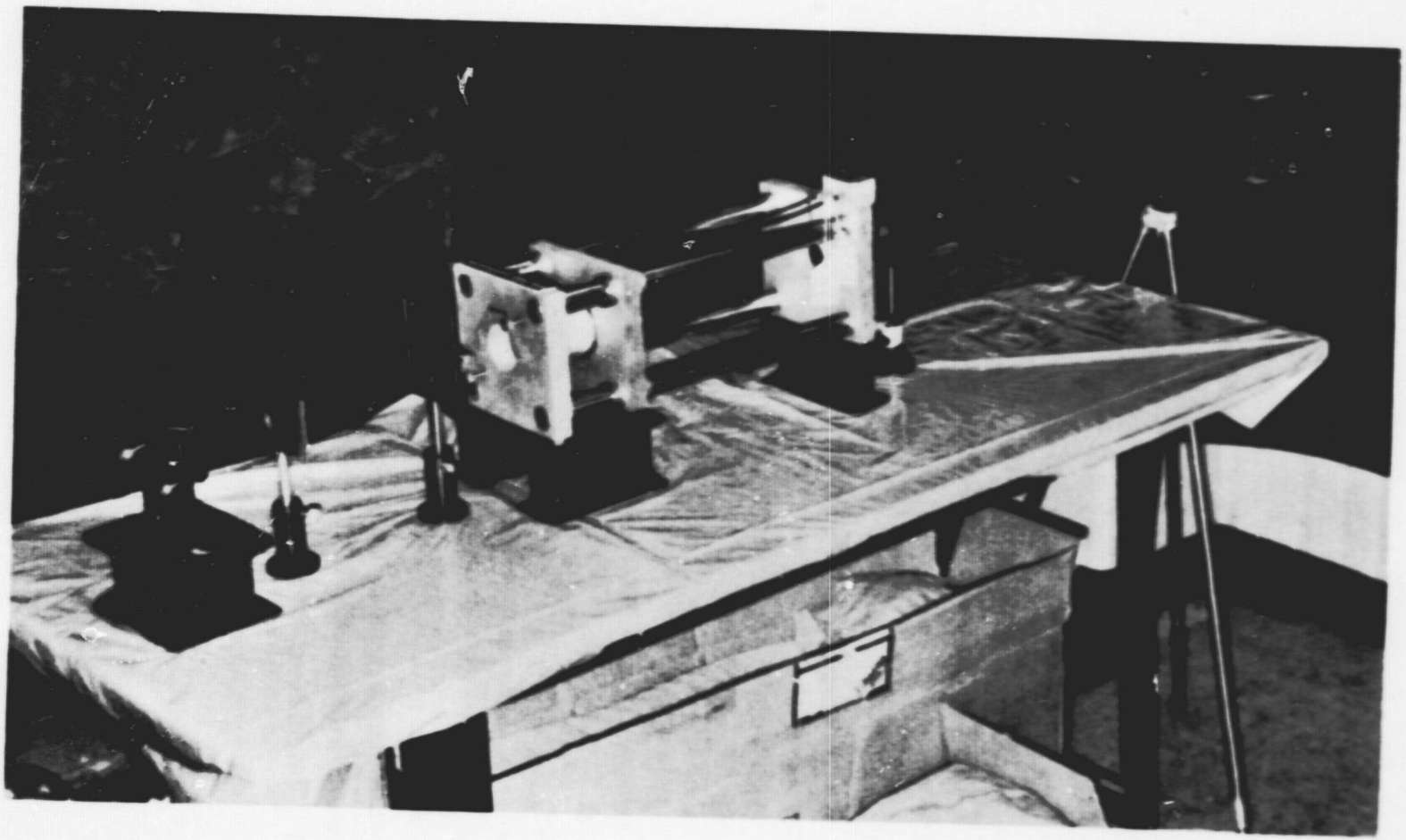

Figure 3.9 Photograph of the Fabry-Perot measurement setup. Devices on table from left to right are the folding mirror, an iris, a field lens, the Fabry-Perot mirror mount, the focusing lens and just behind the table is the covered recording film.

4. PHOTOMULTIPLIER TUBE OVERLOADING AND NORMALIZATION BIN SMOOTHING IN THE RAYLEIGH SCATTERING REGION

4.1 *Introduction*

In Chapter 2, the following expression was developed for the average sodium concentration in a range bin i:

$$\bar{\sigma}_i = \frac{\sigma_\pi(\pi)(z_i + \Delta z/2)^2 \bar{\sigma}_R}{\sigma_{eff} z_i^2 \bar{T}_i^2} \frac{N_i}{N_R} \tag{4.1}$$

Note that the return from a bin in the Rayleigh scattering region, N_R, appears in the expression. There are two criteria to be considered when selecting an altitude at which to normalize the photocounts returned from the sodium layer. First, the altitude must be high enough that only a negligible amount of light is attenuated from the beam as it propagates from the normalizing altitude to the bottom of the sodium layer. Secondly, the returns from this region must be due to Rayleigh scattering. This is necessary since Rayleigh scattering is ordinarily the last loss mechanism operating on the beam until it reaches the sodium layer. Also, Rayleigh scattering is well understood and expressions which relate the returns via that mechanism are easily obtained.

This chapter will deal with issues related to choosing, if possible, a range and an associated bin value to normalize the returns and calibrate the photocounts. Section 4.2 discusses the predicted nature of the Rayleigh returns. Section 4.3 mentions problems due to photomultiplier tube (PMT) overloading from this region. Section 4.4 presents a method to smooth the selected range bin to reduce errors contributed by noise.

4.2 *Returns from the Rayleigh Region*

An expression for the returns from an altitude where Rayleigh scattering is the dominant scattering mechanism was developed in Chapter 2 and is given by:

$$N_R = \frac{N_L A_p \bar{T}_R^2 \eta \bar{\sigma}_R \Delta z \sigma_\pi(\pi)}{\bar{z}_R^2} \tag{4.2}$$

The terms N_L, A_p, η and Δz will be constant with height. Two terms, $\bar{T}_R$ and $\sigma_\pi(\pi)$ vary slowly with height and can be considered constant over the interval of altitudes under scrutiny here. The average atmospheric density term $\bar{\sigma}_R$ follows closely to the following exponential relationship:

$$\bar{\rho}_R = \rho_o e^{-z_R/H} \tag{4.3}$$

where ρ_o is the density at an altitude of zero and H is the atmospheric scale height. Lumping the terms which don't vary with height into a constant K, equation (3.2) can be rewritten as:

$$N_R = \frac{K}{z_R^2} e^{-z_R/H} \tag{4.4}$$

Over a narrow altitude range the inverse altitude squared relationship will be dominated by the exponential. Therefore, returns from the Rayleigh region should demonstrate a strong exponential decay with height. Figure 4.1 demonstrates returns from the Rayleigh region showing this predicted exponential response.

4.3 *Photomultiplier Tube Overloading*

With the addition of the 1.22-m telescope to the Urbana Lidar system, an increase of a factor of 5 over the 0.38-m telescope has been observed in the photocounts from the Rayleigh region [*Rowlett and Gardner*, 1979]. This increase in signal has been significant enough to cause the system PMT to overload. The overloading is characterized by returns much reduced or even nulled out over a period of time followed by a recovery interval where the counts rise to their expected value. The null or reduced response period depends on the strength of the overloading signal. Figure 4.2 depicts a plot of the unfiltered photocounts vs. altitude of a profile taken with the 1.22-m telescope. The returns show a null portion up to the 25 km range followed by the recovery interval up to approximately 40 km after which the returns follow their usual response. Clearly, there is no exponential decay observable in the lower regions which means that this profile cannot be calibrated.

Fortunately, the overloading is not always so severe. Figure 4.3 shows another profile of unfiltered photocounts plotted vs. altitude. The region below 30 km shows erratic and reduced returns until reaching the 28 km level where an exponential decay is clearly evident. By selecting a bin in the 28 km to 45 km interval where Rayleigh scattering is dominating the returns, the profile can be calibrated. The following section presents a method for choosing this altitude.

4.4 *Rayleigh Normalization Bin Selection and Smoothing Technique*

Figure 4.4 is a plot of the photocounts vs. altitude for a profile

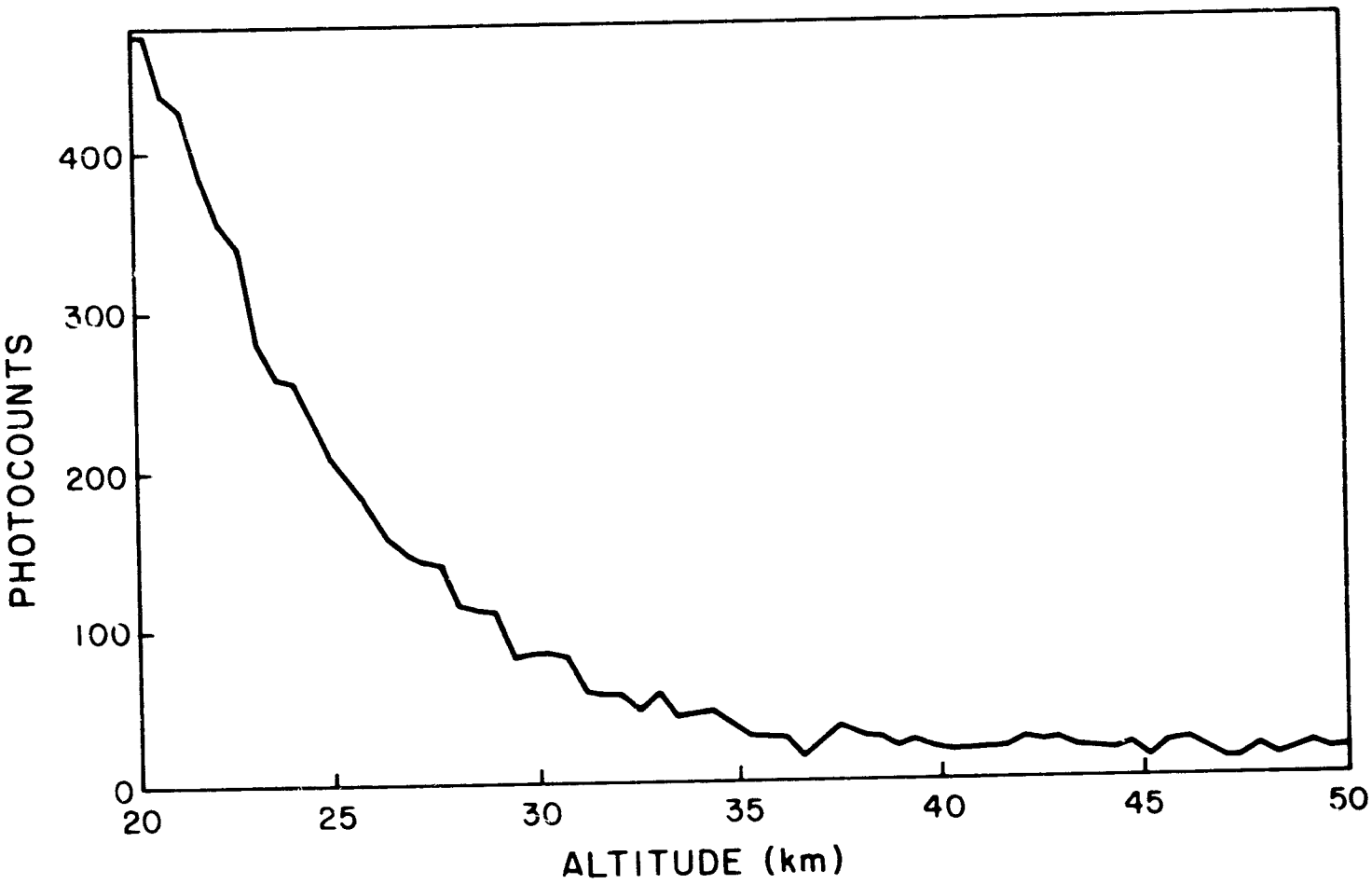

Figure 4.1 Sodium lidar returns from the Rayleigh scattering region of the atmosphere showing a characteristic exponential fall-off into the system noise level.

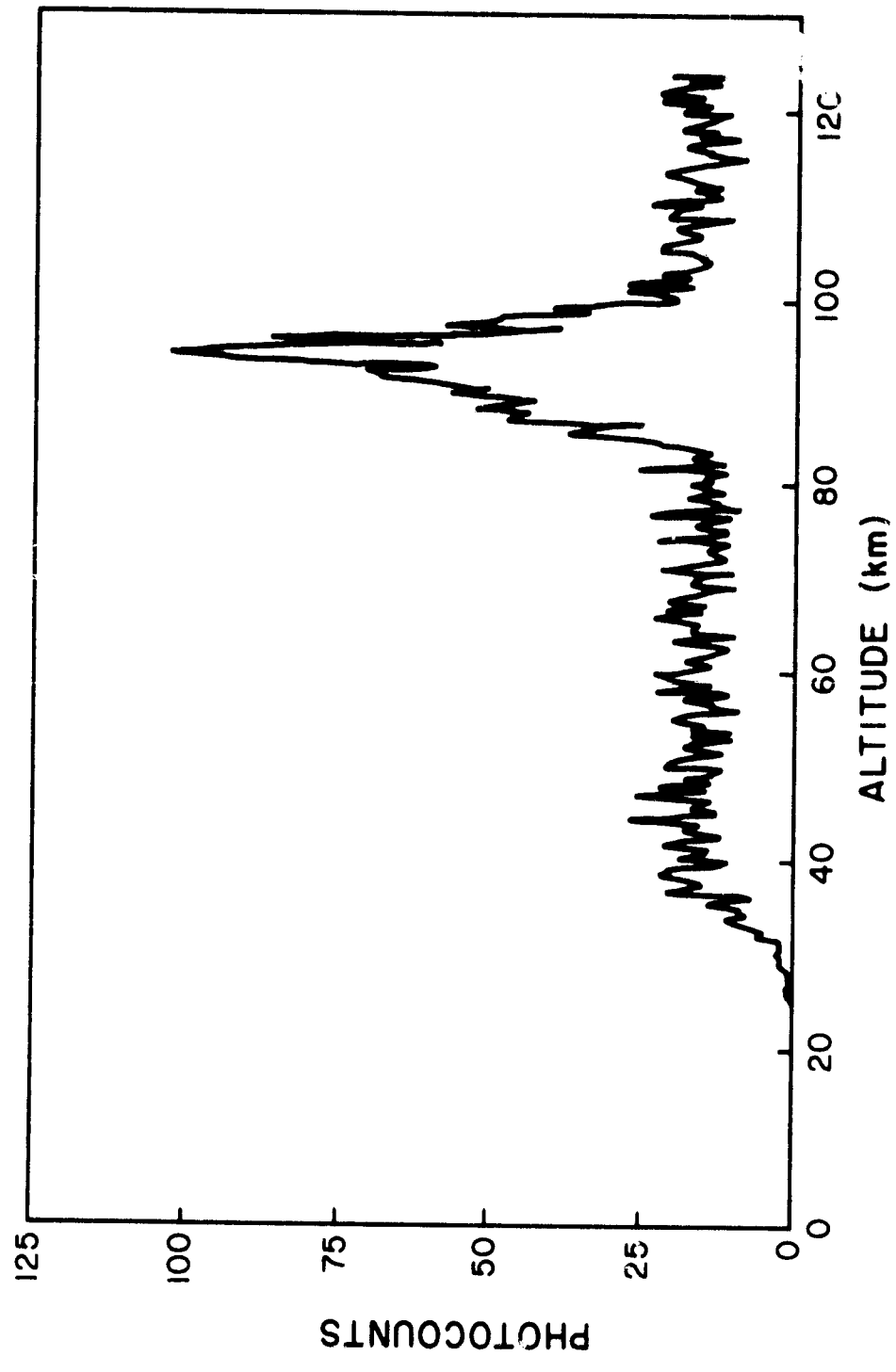

Figure 4.2 Sodium lidar returns showing extensive overloading of the photomultiplier tube in the Rayleigh region. Clearly, no region of the returns shows evidence of Rayleigh scatter implying this profile cannot be calibrated.

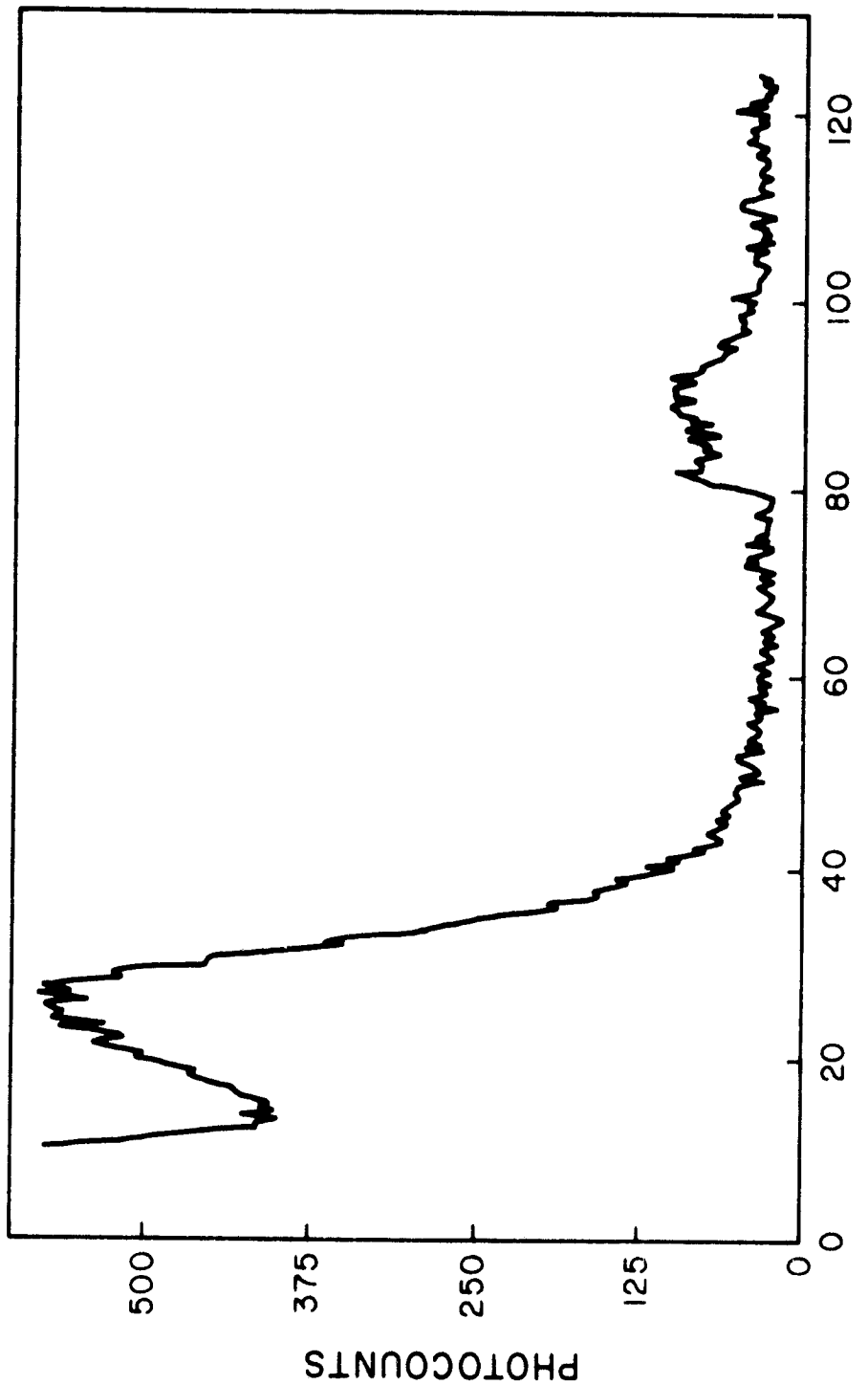

Figure 4.5 Solid: Lidar returns showing [illegible] at wavelengths
[illegible] in the absence of aerosols are exhibiting exponential
decay, allowing the calibration of the profile.

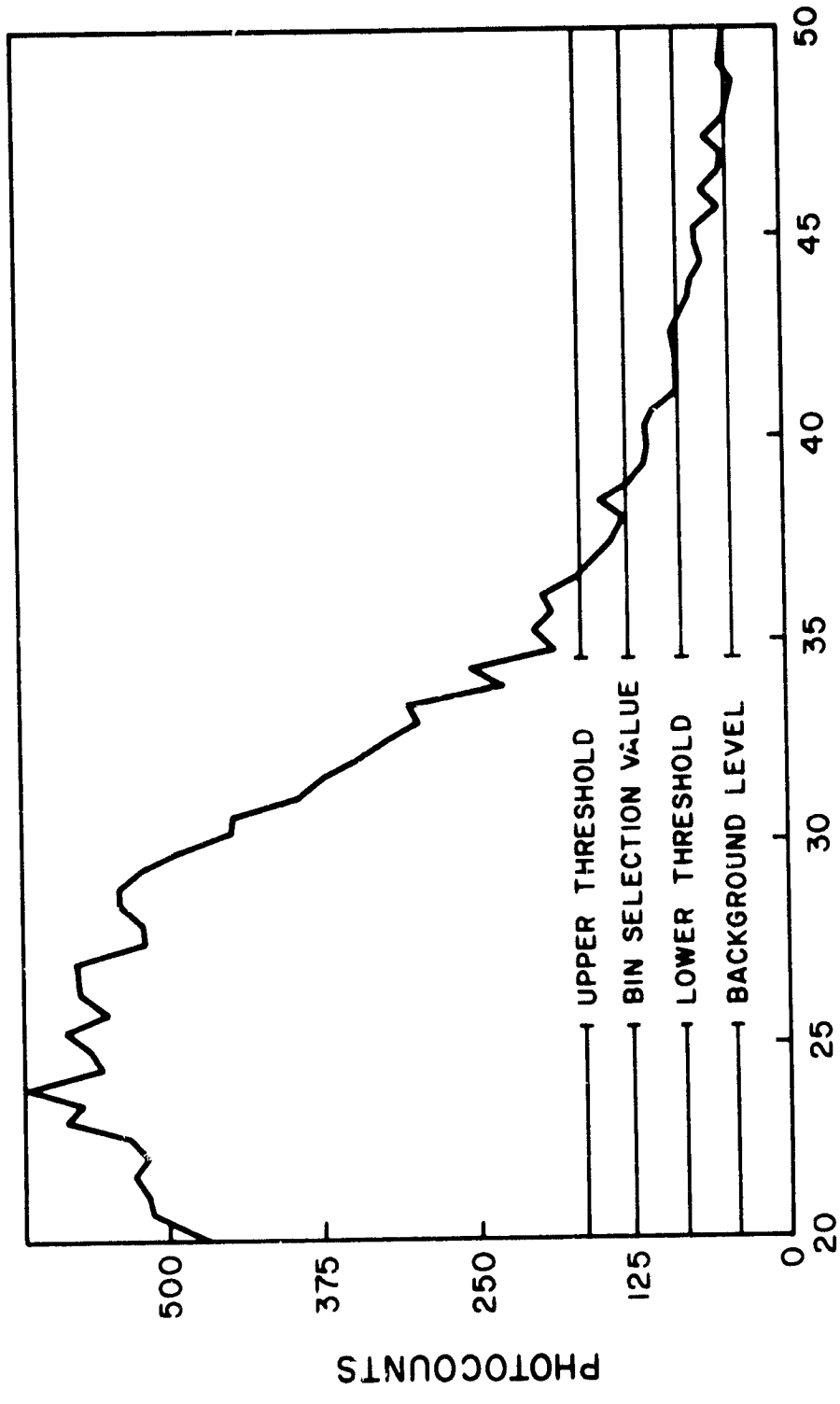

Figure 4.4 A typical plot of photocounts showing some signs of overloading and the criteria used for searching for and selecting an appropriate bin with which to calibrate the profile.

which has an interval strongly dominated by Rayleigh scattering. Clearly some amount of noise is present in this signal as the deviation from a purely exponential decay reveals. To minimize the effects of this noise, some sort of smoothing needs to be done on the Rayleigh scattered bin values. The following presents a least squares fit method of performing the desired smoothing.

Equation (4.4) expresses the number of photocounts received at a height z_R as a function of that height. By multiplying each side of (4.4) by z_R^2 and taking the natural logarithm of each side, (4.4) now becomes:

$$\ln N_F z_R^2 = \ln K - \frac{1}{H} z_R \tag{4.5}$$

Equation (4.5) exhibits a linear relationship between $\ln N_F z_R^2$ and the altitude z_R. Therefore, a least squares fit can be done for these two quantities providing the desired smoothing.

As discussed previously, not all of the returns are due to Rayleigh scatter. Range bin values which are dominated by noise or which show signs of overloading effects in the PMT cannot be used in this fit. A computerized method to examine the returns and choose and smooth an appropriate bin is used in this calibration technique. In this method a background noise level is first computed by averaging the returns in several bins which are due to noise. Two thresholds are now computed. An upper threshold at four times the background level and a lower threshold at two times the background level. The returns within these threshold levels are examined and the altitudes where the returns are at a level of three times the background counts are found. All pertinent levels and thresholds have been indicated for the profile in Figure 4.4. The altitudes at which the count is three times the background count are averaged to determine the height at which the normalization is performed. Next, the five bins on either side of the chosen bin are curve fitted and a smoothed value for the normalization bin is computed.

5. EXPERIMENTAL RESULTS AND ERROR ANALYSIS

5.1 *Experimental Results*

In Chapter 2, an expression relating the photocounts to the sodium concentration was developed, the final form of which is given by equation (2.45). Chapter 3 provided the necessary information to calculate a value for the effective cross section. The value of the Rayleigh range bin, its altitude, and the number density of the atmosphere were the topics for Chapter 4. With the addition of the raw data which provides values of altitude and range bin photocounts, equation (2.45) can be evaluated. These results are the topic of this section.

As mentioned in Chapter 1, a seasonal variation in sodium column abundance is defined as the number of sodium atoms contained in a column extending from the ground to the top of the atmosphere and having a unit area cross section. The column abundance reported in the past shows an increase in the winter values over the summer values. This feature is evidenced by comparing Figures 5.1 and 5.2. Figure 5.1 is a calibrated profile from the June 24-25, 1979 data set. Note that the layer extends from 80 to 100 km with a peak concentration of 1.5×10^{9} m^{-3} at an altitude of 85 km. Figure 5.2, the winter profile was taken January 18-19, 1980 and extends over the same 80 to 100 km range. The peak of the layer now occurs around 88 km and has a value of 7.5×10^{9} m^{-3}. Most of the increase in sodium atoms is found on the topside of the layer. *Hlavka and Bradford* [1971] have also observed this occurrence.

Figure 5.3 illustrates the average nightly column abundance against the month of the year. The data was taken during a period extending from November, 1977 to January, 1980. Examination of this figure shows some interesting features. First, the abundance in the winter months of December, January and February are a factor of 5 to 7 times larger than the abundances observed during the summer months of June and July. Note also that the cyclic nature of the variation is fairly smooth. In other words, approximately equal amounts of time are spent in the enhanced and depleted portions of the cycle. This smooth variation suggested that the data be fitted, by means of a least squares error method, to a sinusoid. The functional form of the sinusoid is given as $3.75 \times 10^{13} \sin(2\pi(x - 9.85)/12) + 4.55 \times 10^{13}$ m^{-2} where x is the month. The value of x ranges from 0 to 12 with 0

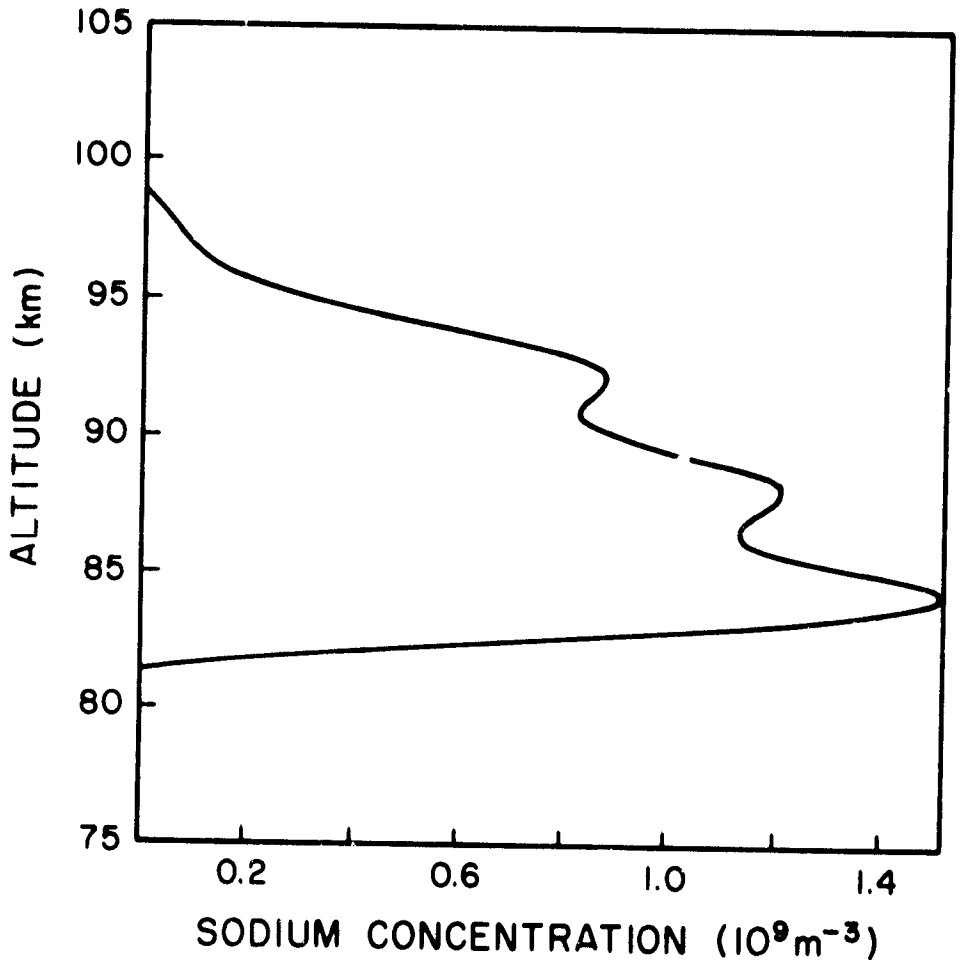

Figure 3.1 A calibrated profile of summertime data taken on the evening of June 24 and 25, 1979. This particular profile was the fifth one taken that evening and was low-pass filtered with a cutoff spatial frequency of (3.75 km)$^{-1}$.

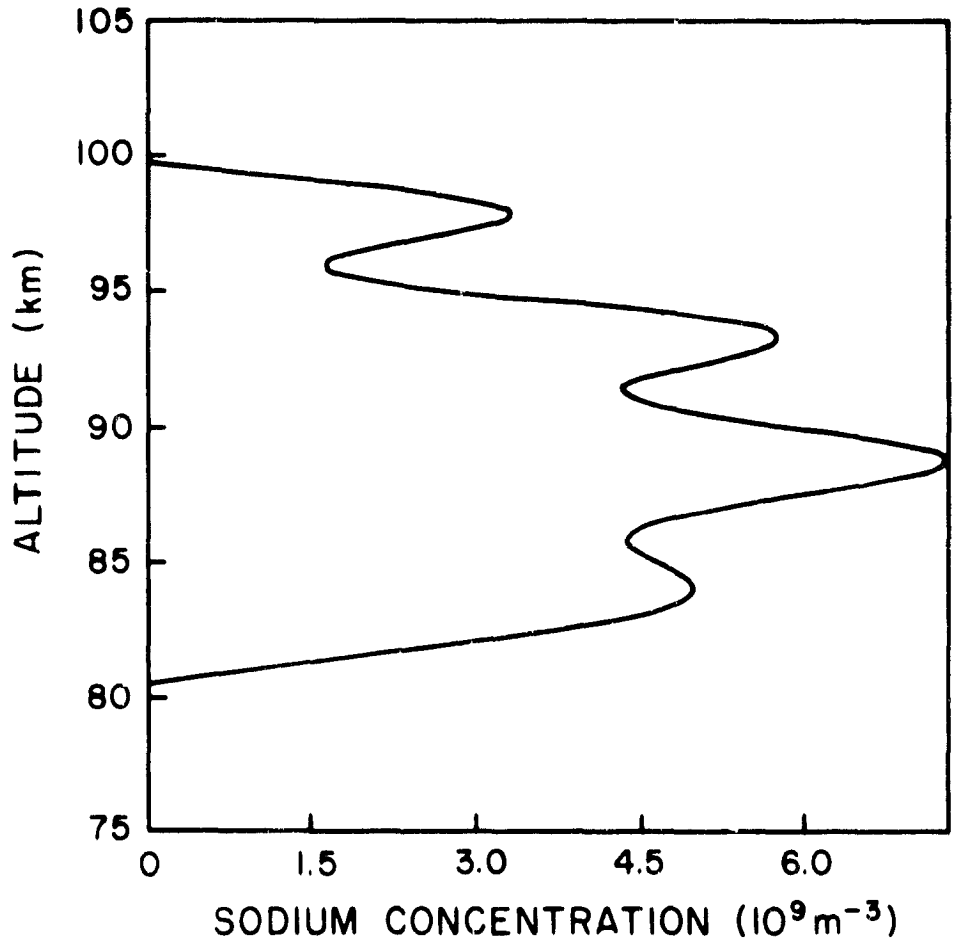

Figure 3.2 A calibrated profile of wintertime data taken on the night of January 18 and 19, 1980. This was the eighth profile observed that evening and was low-pass filtered with a cutoff spatial frequency of $(4.00\ km)^{-1}$.

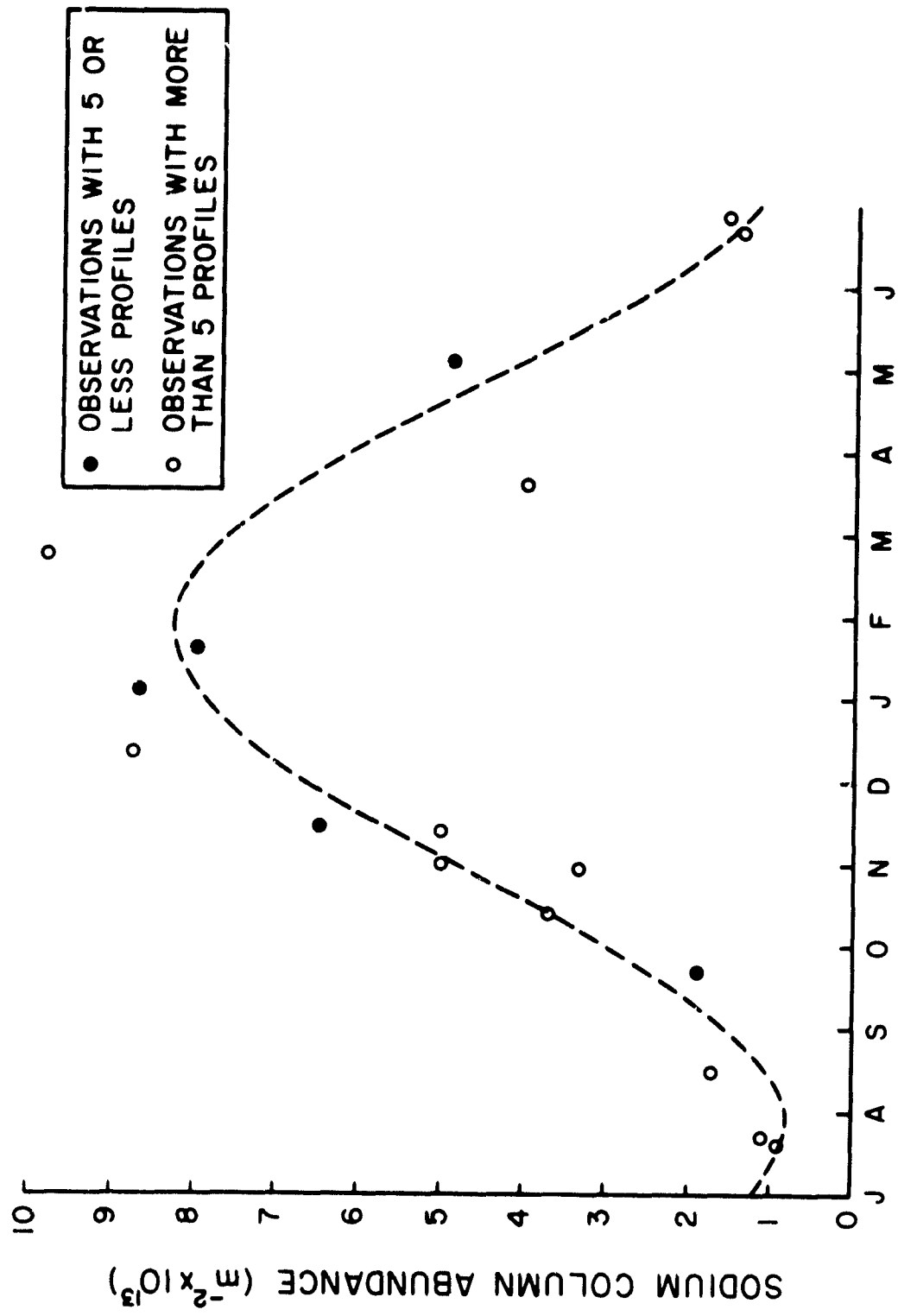

Figure 3.5 Plot showing the seasonal average of the sodium column abundance. The data were fitted via a least-square error method to a sinusoid having a value of 5.75 x 10^{13} $\sin[2\pi(t - 9.85)/12] + 4.55 \times 10^{13}$ m^{-2}. The term t is a variable representing the month. A value of 0 represents the beginning of January while one of 12, the end of December.

representing the beginning of January and 12 the end of December. As can be seen the data fits the curve well although a larger data base would be needed to draw more definitive conclusions. The phase delay of 9.85 corresponds to October 26.

While these results compare well to the past observations reported by other groups on the whole, there are some differences. First, the factor of 5 to 7 increase agrees much more closely with the *Gibson and Sandford* [1971] value of 5 than it does with the *Mejie and Blamont* [1977] value of 4 and the *Simonich et al.* [1979] value of 2. *Simonich et al.* [1979] felt that this factor was related to latitude, larger factors being found at higher latitudes. The latitude of the Urbana system of 40°N and the *Mejie and Blamont* [1977] latitude of 44°N are in close agreement. However, the factor of increase agrees more closely with the English results obtained at a latitude of 52°N. Therefore, the latitude dependence of the factor of increase does not seem to be valid for these results.

Simonich et al. [1979] reported a smooth cyclic variation, however, *Mejie and Blamont* [1977] have observed a much shorter period of enhancement lasting only 2 to 3 months, the rest of the year being somewhat equivalent *Gibson and Thomas* [1971] published a variation similar to this one but having a marginally shorter enhancement.

Finally, the consistency of results as shown in Figure 5.3 yields confidence in the relationship between the calibration of the different evenings of observations. No points, even those with less than 5 profiles averaged, deviate significantly from the rest of the group.

5.2 *Error Analysis*

To perform the error analysis, an RMS mean error will be used. This can be defined as:

$$\Delta\rho_i(f_1, f_2, \ldots) = \left[\left(\frac{\partial \rho_i}{\partial f_1} \Delta f_1 \right)^2 + \left(\frac{\partial \rho_i}{\partial f_2} \Delta f_2 \right)^2 + \ldots \right]^{1/2} \qquad (5.1)$$

where a delta quantity represents the uncertainty of that quantity. Assuming τ_i, $\Delta\tau$, α_i, N_e, τ_{ik}, τ_i and $\sigma_i(\pi)$ have negligible amounts of error, ρ_i becomes a function of τ_{ik}, N_e and $\sigma_{\tau_{ik}}$. Evaluating equation (5.1) using these variables results in:

relation of the profiles to each other should be much more reliable. However, for this tuning error, the relationship between profiles becomes unsure as the tuning randomly varies through the evening.

Table 5.1 Summary of statistics from the October 29, 1978 dataset. The column abundance is directly related to the signal photons and inversely related to the Rayleigh photons. Low numbers of signal photons in profiles 4 and 6 are probably due to drift in the laser tuning since the Rayleigh counts stay relatively constant.

Profile #	Signal Photons	Rayleigh Photons	Column Abundance	% Deviation from avg. abundance
1	2086	30.4	6.3×10^{13}	26
2	1716	35.6	6.3×10^{13}	26
3	1263	31.6	4.6×10^{13}	- 8
4	730	28.2	3.3×10^{13}	-34
5	1446	31.2	5.4×10^{13}	8
6	872	33.5	3.7×10^{13}	-26
7	1056	24.8	4.3×10^{13}	-14
8	1240	33.7	5.1×10^{13}	2
9	1225	30.0	6.1×10^{13}	22
10	1551	28.0	6.9×10^{13}	38
			Avg. = 5.0×10^{13}	

6. SUMMARY AND RECOMMENDATIONS FOR FURTHER WORK

6.1 *Summary*

From the lidar equation, an expression was developed to calculate the sodium concentration from observed photocounts collected with the Urbana lidar system. The main unknown in the equation was the laser linewidth. A Fabry-Perot interferometer was designed and constructed to perform this measurement. The laser linewidth was measured to be 6 ± 2.5 pm. Some problems in calibrating the photocount vs. altitude data were encountered from photomultiplier tube overloading. A method for selecting a normalization bin found in the Rayleigh scattering region was developed. With this information, past data were calibrated. The data showed a strong winter enhancement in the sodium column abundance of a factor of 5 to 7 over the summer values. The data were fitted with a cosine curve with good results. The calibration is accurate to within 50%, approximately.

6.2 *Recommendations for Further Work*

6.2.1 *Further linewidth studies.* A more rigorous study of the linewidth and its variability needs to be undertaken to reduce the uncertainty in the calibration. Variability studies through an evenings' run and on a night-to-night basis would be beneficial in ensuring an accurate calibration. An even better arrangement would be to monitor continuously the linewidth and record its values throughout the evening. Some sort of linear detector array would be best since it must have a quick response time. If photographic methods are continued, some sort of alternative to Polaroid film should be used. The film should be able to accept a wide range of pattern intensities to cope with the changing output energies.

6.2.2 *Center frequency monitor.* As was discussed in Chapter 5, drifting of the laser center frequency is another cause of error which should be eliminated. This parameter will need to be controlled and monitored during data collection. Either an interferometry or cell absorption method should be used.

6.2.3 *Gating or shuttering of photomultiplier tube.* In order to eliminate the PMT overloading, the PMT must either be gain switched electronically or have its input mechanically blocked by a shutter during the low altitude returns interval. Electronic gain switching will require modification of the PMT housing as well as the external switching and timing

circuitry. A rotating shutter would require a motor equipped with a propeller-like shutter as well as position sensing and timing circuitry. This is a significant problem because some photocount vs. altitude profiles cannot be calibrated due to the severity of the overloading.

6.2.4 *Larger data base of calibrated profiles.* In order to achieve more confidence in the seasonal fluctuation of sodium, a larger data base is needed, especially from January to June. This information can be had at no loss to other investigative objectives.

APPENDIX I

Operating Procedures for the Lidar Transmitter

The following is a step-by-step instruction set for aligning and operating the Urbana dye laser.

1. Prepare and install a new set of flashlamps.
2. Prepare a concentrated solution of the Rhodamine 6G dye.
3. Using the Simer pump on the stand holding the water deionization system, pump the cooling water from its reservoir into the nalgene holding tank. Using acetone, clean out the cooling water reservoir and paper towel dry. Be careful not to inhale the acetone fumes. Replace the cooling water reservoir and open up the stopcock at the bottom of the holding tank. Keeping the drain valve closed on the deionizer, open the inlet valve to obtain a good water flow through the deionizer. Slower flows haven't proven to increase the waters resistivity.
4. Remove the fire bricks which form the oven for the sodium resonance cell. Remove the cell and look at the base to see if there is an adequate supply of sodium deposited on the glass. If there is a sufficient amount, one should observe a silver-blue coating around the glass that obscures the sodium channels within. If the coating is not very thick and allows easy viewing of the sodium channels, more sodium needs to be released from the channels. To accomplish this, obtain a low voltage, high current ac power supply capable of an output of 9 to 10 amps. Notice that the cell has three wires exiting the bottom of the cell. Each of the outer wires corresponds to one of the sodium channels. The center wire is common to both. When beginning with a new cell, use only one of the channels to release sodium until it has been used up, then switch to the second. It is therefore advantageous to mark the lead of the channel which has been used most recently. Connect the power supply to the center lead and the proper outer lead and turn the power on to the supply. Begin at zero current and increase slowly to nine amps. Keep the current on until there is a good deposit of sodium on the glass. This should take 20 to 40 seconds depending on the amount of use the channel has experienced. Replace the cell in the

oven and turn the heater on to a setting of 55 on the variac. Monitor the temperature closely, not allowing temperatures greater than 150 C. Temperatures greater than this cause excessive decay of the cell. If time is short the variac can be turned up higher to get the oven to 150 C more quickly, but should then be turned back down again towards the 55 setting. The cell should be positioned inside the oven in such a way that will allow the laser beam to enter through the oven window, pass through the center of the cell and out the oven's back window.

5. Turn on the sodium arc lamp and adjust both it and its associated focusing lens to image the pinhole onto the entrance slit of the spectrometer. Check to see if the sodium doublet is well defined and bright. The eyepiece of the spectrometer will need to be adjusted to form well defined lines. If the sodium doublet is not bright enough to see clearly, readjust the focusing lens and arc lamp.

6. Drain any old dye which may be in the dye reservoir. This can be done by closing the valve on the side of the reservoir rack which leads back into the dye flow system. Afterwards, open the other valve which leads to the free drainage hose. Insert the drainage hose into a container capable of holding the amount of dye in the reservoir. On the front panel, flip the switch under the amber light to the on position. The dye should now be flowing into the drainage container. After all the dye has been removed, turn off the switch and rinse the reservoir with ethanol to remove any residue. It would be wise to wear gloves so that contact with the Rhodamine 6G dye will be minimized. Turn the switch back on again and drain out the ethanol which was used to rinse the reservoir. Shut off the drain valve and replace the drain hose to its storage position. Reopen the valve which leads back into the dye flow system. The dye filter should now be emptied. There are two ways to do this. First, if the dye filter is known to be fairly clean, place a container of at least 600 ml volume beneath the dye filter and open the wing valve at the bottom of the unit. Turn the pump to the on position which should cause the dye to empty out. When finished, turn off the pump and close the wing nut valve. If the filter is dirty and needs replacement, again place the container beneath the dye filter and open the wing valve. Using the wrench kept on the side of the reservoir rack, loosen the bolt on the top of the filter. As the dye

filter container separates from its holder, dye will begin to flow into the vessel which is holding the discharged dye. Allow enough dye to drain out to allow the dye filter container to be comfortably threaded out of the dye flow system apparatus. The wound filter can now be accessed and replaced if necessary. To empty the dye in the dye rod and the tubing which connects it to the pump, locate the hose which enters the front panel of the dye flow system. Placing a beaker or other suitable container beneath this hose, remove the hose from its fixture and allow the fluid in it to gravity drain out.

7. Refill the dye reservoir with new solvent. The mixture ratio is 1 part water to 1 part ethanol. Normally 95% ethanol is used, however purer percentages of ethanol can be used. The normal amount of solvent used for a data run is 16 liters. This would correspond to 8 liters of water and 8 liters of ethanol. When the solvent has been added, the pump can then be turned on. This allows for the air bubbles trapped in the system to work their way out of the flow system. To turn the pump on, flip the switch under the amber light on the pump control panel to the on position. The pressure should begin to build as will be evidenced by the front panel gauge. When the red light goes out, the pressure has exceeded the threshold point at which the safety cutoff will shut down the flow system. Now return the switch under the amber light to the off position. The amber light should remain on and the dye should begin flowing through the system. Next, add in the concentrated dye mixture at a rate of 30 ml dye mix to 1 liter of solvent. A 16 liter solvent solution corresponds to 480 ml of concentrated dye mix. Finally remove the 1, 3, 5, 7, cyclooctatetraene (COT) from the freezer and add it to the solvent at the rate of 0.2 cc per liter of solvent. Therefore, for a 16 liter solution, 3.2 cc of COT would be added. This is best done with a syringe and hypodermic needle. Gently stir the whole solution with a stirring rod. It will probably take 5 to 10 minutes before the solution has mixed well with the dye flowing.
8. Remove the flask that serves as a trap in the vacuum system. Empty any ablation product which might be in it. Periodically rinse it with acetone or ethanol and allow it to dry. Using a paper towel, remove the old vacuum grease around the flask's mouth and from its stopper.

Replace it with a fresh thin coat of vacuum grease on the contacting surfaces. When the vacuum system is first turned on, this stopper may need to be held in place until the vacuum begins to suck it down on its own.

9. If there is enough water in the cooling water reservoir to start the pump, now is the time to do so. Place the hoses in the water and after checking to make sure all hoses around the flashlamps have been reconnected and the clamps on them removed, turn on the pump. If the pump does not prime, place a rubber bulb in the water and fill it with water. Keeping both it and the inlet hose under water, force water into the inlet hose until a solid column of water reaches and goes through the pump. The pump should now work at this time.
10. Remove the cover for the bi-elliptical cavity and check to make sure the dye rod is oriented properly with respect to the cavity. It should be positioned along the common focus axis. This provides a rough alignment of the dye rod along the optical axis.
11. Remove the optics from the rail and turn on the HeNe alignment laser. Adjust the laser so the beam passes through the center of the quartz windows on each side of the rod. The dye should be flowing at this point since the beam propagates through the rod differently when there is no flow. An adequate way to center the beam in the windows now follows. First, remove the pinhole from in front of the alignment laser. This is done to allow the HeNe laser to be moved without having to readjust the pinhole. Next, move the front end of the HeNe laser (the end nearest the cavity) to center the spot in the window horizontally. If the vertical adjustment is off, check to see if the beam is at the same height above the rail for the length of the rail. If that adjustment is not correct, level the beam using computer cards underneath the alignment laser. When this is done, recenter the beam horizontally by moving the front end of the laser, as before. The beam should not be too far from the center of the nearest window. Undo the set screw which controls the height positioning of the rod and adjust the rod to center the beam in the window. Retighten the set screw and perform the same adjustment on the back window. The horizontal adjustment on the back window will most likely be off at this point, but the window can still be vertically centered. Now, note to which side of the back window the beam is positioned. Move the back end of the laser to the same side. The

amount moved will depend on the distance from center. Adjust the front end of the laser to center the beam on the front window. Check the position of the beam on the back window and make more adjustments as necessary. After completing the centering process, the bi-elliptical cavity may need to be readjusted so that the dye rod is still at the common focus and not in physical contact with the cavity. This is done by loosening the four bolts which hold the cavity to its black support frame, centering the cavity with the dye rod and retightening the bolts. Ensure that once the dye rod is centered, the hoses facing the dye rod will not be jostled or moved around. Even slight movements can destroy the alignment. This can be seen by moving the hoses and watching how the beam moves on a viewing screen at the back of the optical rail.

12. Place the grating as far back as it will go on the optical rail. If it's not known whether or not the grooves are oriented vertically, they should be checked for proper alignment. To do this, first position the mount so that the beam is retroreflected back into the laser. Now, rotate the grating so that the angle of incidence is changed. Soon, the first order of diffraction should appear somewhere around the dye cell. If the grooves are vertical, the first order too will retroreflect back into the laser. If not, the grating should be rotated in its mount until this condition is met. Now turn the mount so that the first order on the other side of normal incidence comes into view. This diffracted beam should also retroreflect if the grooves are properly aligned. Make adjustments as required so that all three beams will retroreflect when the mount is rotated on the optical rail. Next, carefully examine the grating and choose an area, at least 5 mm in diameter, that is fairly clean and unmarked. Position the mount so that the laser beam is incident on this spot. Orient the mount's angle to this beam so that the first order of diffraction is retroreflected back into the laser. The angular positioning micrometer should be positioned at a setting of at least 300 mils, since this will need to be readjusted later. The mount should be clamped securely into place, and fine adjustments made with the micrometers to re-center the beam on the alignment laser. The pinhole should be in position in front of the laser to make the adjustment as accurate as possible.

13. Place the mirror that makes up the mirror grating combination in front of the grating. Select a good clean position on this and have the beam strike the mirror there. Securely tighten it to the rail and adjust the micrometers so that the beam is retroreflected. This adjustment is critical and should be done with care. The grating may need to be blocked off so that its reflections will not hinder the mirror alignment.
14. Put the output mirror in place. Clamp it to the rail and adjust the micrometers so that it retroreflects. Usually, some faint spots, originating from the mirror grating combination, will be visible and can aid in this process.
15. Between the output mirror and alignment laser, place a glass slide and position it so that the HeNe beam is reflected towards the beam splitting table located on the sides of one of the 40 Mlz transmitter cavities. Position the beamsplitter mirror so that it guides the beam to the input slit of the spectrometer. The throughput from the beamsplitter should be guided via the total reflector through the center of the sodium resonance cell.
16. Subtract 180 mils from the angular adjusting micrometer head on the grating. This converts the alignment from 632.8 nm to 589.0 nm.
17. Block off the alignment laser.
18. Turn on the water spigot on the mezzanine which cools the dye. Just a good steady flow of water should be sufficient.
19. Replace both the bi-elliptical cavity cover and the wooden cover which goes over the whole central assembly.
20. Turn on the vacuum pump, making sure the manometer's stopcock is turned so that both sides of the column are at the same pressure. As mentioned before, the stopper in the flask trap may need to be held down until the vacuum is well started. Allow this to run for about a minute so that a good vacuum is developed. Once a good vacuum is present, turn the stopcock on the manometer to isolate the two sides of the column. This provides the manometer with a vacuum reference to measure system pressure with.
21. Turn on the nitrogen supply at the tank and adjust the diaphragm so that the line pressure gauge just barely shows some pressure. Open up

the line to the flashlamp system and allow the manometer to come to a reading of four torr. This valve should only be handled by the black plastic to avoid shocks when the high voltage is on. The shocks are not dangerous but do provide some discomfort.

22. Turn on the pulsing equipment sitting on the table nearest the output end of the laser. There are two units which perform the pulsing. The high voltage pulser is a metal chassis with a transformer mounted on top. The power switch and red indicator light are located on top. The second unit is an external trigger unit in a small metal chassis box. This has the time between pulse adjustment on it, which should be set on the two second position. Turn the black slide switch on the high voltage pulser to the external trigger position and gaze into the bielliptical cavity to try to see if the flashlamps are breaking down. If you cannot see the pulsing, listen for a snapping sound which will also indicate whether or not the pulser is working.

23. The high voltage is now ready to be applied. Quickly recheck to see if the dye is flowing, the cooling water is on and flowing, the dye cooling water is on, and that the vacuum system is on with pressure at four torr. Plug in the power supply and switch it on with the variac in the "zero voltage" position. Slowly increase the voltage until the lamps begin breaking down. This should occur around 13 kV. Continue the voltage increase until lasing is observed. The easiest place to look for lasing is on the grating.

24. Adjust the up and down positioning micrometer on the grating to try to obtain a good symmetrical lasing spot. As you near the optimum setting the energy per pulse will increase. The voltage may need to be turned down to keep the grating safe from danger as the energy increases. When the spot resembles a low order spatial mode, gaze into the spectrometer and adjust the angular micrometer to tune the emission onto the D_2 line. The D_2 line is the right side of the sodium doublet looking into the spectrometer. Now, reduce power until the system is barely lasing. Make final adjustments on the up and down setting of the grating to optimize the spot configuration. If a ring or doughnut spot occurs, the laser is in good alignment and will probably work well. Don't use too much time trying to obtain this pattern, since it doesn't always occur. The laser will also work well if a good Gaussian spot is obtained.

25. Turn off the pulser and reduce the high voltage power supply to zero and turn it off as well. Place the resistive discharge probe on top of the resistor bank and discharge the capacitor and power supply. You can watch the voltage reading on the power supply to see when the voltage has decayed to zero. Place the dead short on top of the resistor to get rid of any residual charge. Unblock the alignment laser and remove the wooden cover. Put the etalon in place and clamp it securely. As always look first to be sure a good clean area of the optics is being utilized. Adjust the etalon so that the laser beam is reflected to a spot just between the dye rod and the flashlamp adapter on the bakelite plate. The beam should be at the same height as the center of the window. There should be a spot on the bakelite to mark this position.
26. Block off the HeNe beam once more and replace the wooden cover. Increase the system pressure to 7 or 8 torr. Switch on the pulser and look or listen for evidence of pulsing. Turn on the power supply and increase the voltage until good lasing is observed. The need for caution concerning damaging optical energy too high energy densities is reduced with the etalon in the system. The optics have proven to be safe even at maximum voltage.
27. Look into the spectrometer and observe the laser emissions' spectral qualities. There should only be one thin narrow line somewhere close to the P_2 line. Sometimes a faint line will occur one or two free spectral ranges of the etalon away from the main line. This is due to lasing off of the mirror in the mirror grating combination. Not much can be done with this problem. If other emissions are present, return to the grating alignment stage and begin again from there. Now look through the spectrometer and see if the laser line is close to the P_2 line. Under normal circumstances, it should look to be right on the P_2 line. Gaze into the resonance cell and see if scattering is observed in the cell. If not, note the current position of the angular adjustment micrometer and begin moving the micrometer in steps of about 1 mil in one direction, looking for scattering after each new adjustment. After moving 10 mils away from the center position, return to the original position, just noted, and go in the other direction in 1 mil

steps. Again, if no scattering is observed after moving 20 mils in this direction, return to the 10 mil position on the other side of the starting point and search through 10 more mils in this direction. If no scattering has yet been found, look back into the spectrometer and adjust the micrometer to recenter the laser line on the D_2 line. This is the procedure to follow if the laser line was originally displaced from the D_2 line. Note this new position and restart the search process. If again no scattering is found, return to step 25 and repeat those procedures, perhaps trying a new spot on the etalon. Once you have found scattering, locate the positions where scattering is just barely observed. Make the final setting to be the middle of these two positions. Usually, there is a spread of 1 to 2 mils in these positions.

28. Remove the glass slide from the rail and place the 45 degree mirror into place, clamping it down securely. Adjust the micrometers on this mirror to center the beam on the marks on the hatch. Open the hatch at this point being careful of the high voltage. You may want to discharge the system if so desired. The laser is now ready to be aligned with the telescope.

29. As the telescope/laser alignment is being performed, place a silvered mirror behind the 45 degree mirror and direct this residual beam through the sodium cell and into the spectrometer as before. Recheck the tuning every 10 to 20 minutes and recenter the micrometer between the "just scattering" positions. If pulsing becomes irregular, adjust the pressure upwards if spontaneous shots are occurring and downwards if expected shots don't occur.

30. To shut down the system, turn off the pulser, turn down the high voltage power supply to zero and switch it off. Unplug the power supply, then discharge the capacitor and power supply as mentioned before. Turn off the nitrogen and allow the column of fluid to come to equilibrium. Turn the stopcock to the horizontal position so that both sides of the column are at the same pressure. Turn off the vacuum system and then the nitrogen tank. Remove the nitrogen hose from the valve which is used to adjust the residual pressure in the vacuum system. Open it slightly and allow the flashlamps to return slowly to atmospheric

pressure. This should reduce the probability of leaks occurring in the flashlamps. Cover the optics with plastic bags, being careful the plastic does not touch the optics surface. Turn off the sodium cell heater and arc lamp supply. Turn off the cooling water to the dye. Close the hatch and tie it down. Turn off the dye pump by pressing the black button below the red lamp until the amber lamp goes off, then release it. Turn off the flashlamp cooling water pump. Finally, turn off the bench power strips.

REFERENCES

Blamont, J. E., M. L. Chanin and G. Megie [1972], Vertical distribution and temperature profile of the night time atmospheric sodium layer obtained by laser backscatter, *Ann. Geophys., 28*, 833-838.

Born, M. and E. Wolf [1959], *Principles of Optics: Electromagnetic Theory of Propagation, Interference and Diffraction of Light*, Pergamon Press, Oxford.

Bowman, M. R., A. J. Gibson and M. C. W. Sandford [1969], Atmospheric sodium measured by a tuned laser radar, *Nature, 221*, 456-457.

Chamberlain, J. W. [1961], *Physics of the Aurora and Airglow*, Academic Press, New York.

Gibson, A. J. and M. C. W. Sandford [1971], The seasonal variation of the night-time sodium layer, *J. Atmos. Terr. Phys., 33*, 1675-1684.

Gibson, A. J. and M. C. W. Sandford [1972], Daytime laser radar measurements of the atmospheric sodium layer, *Nature, 239*, 509-511.

Gibson, A. J., L. Thomas and S. K. Bhattacharyya [1979], Laser observations of the ground-state hyperfine structure of sodium and of temperatures in the upper atmosphere, *Nature, 281*, 131-132.

Herrmann, U., P. Eberhardt, M. A. Hidalgo, E. Kopp and L. G. Smith [1978], Metal ions and isotopes in sporadic *E*-layers during the Perseid meteor shower, *Space Research, 18*, 249-252.

Hunten, D. M. [1967], Spectroscopic studies of the twilight airglow, *Space Sci. Rev., 6*, 493-573.

Kent, G. S. and R. W. H. Wright [1970], A review of laser radar measurements of atmospheric properties, *J. Atmos. Terr. Phys., 32*, 917-943.

Kinter, T. M. [1977], A Laser Radar System Interface, *M.S. Thesis*, University of Illinois, Urbana-Champaign.

Kirchhoff, V. W. J. H. and B. R. Clemesha [1973], Atmospheric sodium measurements at 23°S, *J. Atmos. Terr. Phys., 35*, 1493-1498.

Measures, R. M. [1977], Lidar equation analysis allowing for target lifetime, laser pulse duration, and detector integration period, *Appl. Opt., 16*, 1092-1103.

Megie, G. [1976], Contribution à l'étude du comportement de l'atmosphère à la mésopause obtenue par sondage laser du sodium, *Ph.D. Thesis*, l'Université Pierre et Marie Curie, Paris 6.

Megie, G. and J. E. Blamont [1977], Laser sounding of atmospheric sodium: interpretation in terms of global atmospheric parameters, *Planet. Space Sci.*, *25*, 1093-1109.

Megie, G., F. Bos, J. E. Blamont and M. L. Chanin [1978], Simultaneous nighttime lidar measurements of atmospheric sodium and potassium, *Planet. Space Sci.*, *26*, 27-35.

McCartney, E. J. [1976], *Optics of the Atmosphere: Scattering by Molecules and Particles*, John Wiley and Sons, New York.

McClatchey, R. A. and A. P. D'Agati [1978], Atmospheric Transmission of Laser Radiation: Computer Code LASER, *Environmental Research Papers No. 622*, Air Force Geophysics Laboratory, Hanscom AFB, Massachusetts.

Mitchell, A. C. G. and M. W. Zemansky [1971], *Resonance Radiation and Excited Atoms*, Cambridge University Press, New York.

Penndorf, R. [1957], Tables of refractive index for standard air and the Rayleigh scattering coefficient for the spectral region between 0.2 and 20.0μ and their application to atmospheric optics, *J. Opt. Soc.*, *47*, 176-182.

Richter, E. S. and C. F. Sechrist, Jr. [1978], Theoretical and Experimental Studies of the Atmospheric Sodium Layer, *Aeron. Rep. No. 79*, Aeron. Lab., Dep. Elec. Eng., Univ. Ill., Urbana-Champaign.

Richter, E. S. and C. F. Sechrist, Jr. [1979], A cluster ion chemistry for the mesospheric sodium layer, *J. Atmos. Terr. Phys.*, *41*, 579-586.

Rowlett, J. R. and C. S. Gardner [1979], Signal Processing of Sodium Lidar Photocount Data, *E.E.L. Publication No. 504*, Radio Res. Lab., Dept. Elec. Eng., Univ. Ill., Urbana-Champaign.

Rowlett, J. R., C. S. Gardner, E. S. Richter and C. F. Sechrist, Jr. [1978], Lidar observations of wave-like structure in the atmospheric sodium layer, *Geophys. Res. Lett.*, *5*, 683-686.

Simonich, D. M., B. R. Clemesha and V. W. J. H. Kirchhoff [1979], The mesospheric sodium layer at 23°S: Nocturnal and seasonal variations, *J. Geophys. Res.*, *84*, 1543-1550.

Teitelbaum, E. and C. F. Sechrist, Jr. [1979], A Microcomputer Control System for the Urbana Sodium Lidar, *Aeron. Rep. No. 88*, Aeron. Lab., Dep. Elec. Eng., Univ. Ill., Urbana-Champaign.

Thomas, L., A. J. Gibson and S. K. Bhattacharyya [1977], Lidar observations of a horizontal variation in the atmospheric sodium layer, *J. Atmos. Terr. Phys.*, *39*, 1405-1409

U.S. Standard Atmosphere [1976], N.O.A.A., N.A.S.A. and U. S. Air Force, Washington, D.C

Van de Hulst, H. C. [1957], *Light Scattering by Small Particles*, John Wiley and Sons, New York.

C-2